2004

Design, Fabrication and Testing of Longitudinal Wind Tunnel Balances for Micro Air Vehicle Applications

Andrew T. Walter

Design, Fabrication and Testing of Longitudinal Wind Tunnel Balances for Micro Air Vehicle Applications

by

Andrew T. Walter

A thesis submitted in partial fulfillment of the requirements for the

MASTER OF SCIENCE
IN
MECHANICAL ENGINEERING

Approved by:

Dr. K. Kochersberger Department of Mechanical Engineering	(Thesis Advisor)
Dr. J. Kozak Department of Mechanical Engineering	(Committee Member)
Dr. A. Ghosh Department of Mechanical Engineering	(Committee Member)
Dr. E. Hensel Department of Mechanical Engineering	(Department Head)

DEPARTMENT OF MECHANICAL ENGINEERING
KATE GLEASON COLLEGE OF ENGINEERING
ROCHESTER INSTITUTE OF TECHNOLOGY

NOVEMBER 2004

Permissions Granted

Thesis Title:

"Design, Fabrication and Testing of Longitudinal Wind Tunnel Balances for Micro Air Vehicle Applications"

Name of author: Andrew T. Walter

Degree: Master of Science

Program: Mechanical Engineering

College: Kate Gleason College of Engineering

I, Andrew T. Walter, hereby grant permission to the Wallace Library at Rochester Institute of Technology to reproduce this thesis in whole or in part. Any reproduction will not be used for commercial use or profit.

Andrew T. Walter

11/16/2004

Date

Abstract

Over the past decade the study of Micro Air Vehicles (MAVs) has generated increasing interest due to their potential military, intelligence and civilian applications. One of the primary obstacles in the development of MAVs is the lack of accurate analytical or numerical methods for determining the performance of a particular design. Experimental methods are more prevalent but are difficult to realize because of the large costs and fragility of equipment needed to capture the very small forces associated with MAVs.

This research presents the design, implementation and testing of two new wind tunnel balances for capturing longitudinal aerodynamic data (lift, drag and pitching moment) from MAV scale models. The first is a modification of earlier work at RIT and relies on simple mechanical principles to capture lift and drag independently. The second, the primary focus of this project, is the development of an entirely new, low-cost, LabVIEW-integrated load cell balance. The balance captures all data simultaneously and provides real-time monitoring of the system and computer logging capabilities. Both balances are tested using simple models and compared to published data. Also, the RIT MAV developed in the spring of 2004 is tested to demonstrate the validity of using the load cell balance to test full vehicles for the emerging RIT Micro Air Vehicle Program. A comparison is made between the experimental results and flight testing experience.

The results of the testing show excellent correlation to published data for lift and drag. Pitching moment results remain ambiguous due to large uncertainty. Several potential causes for pitching moment inaccuracy are discussed and solutions and recommendations are presented to correct them. Despite this, the balances are shown to be excellent, user-friendly and low-cost tools for gathering accurate aerodynamic data from MAVs

Acknowledgements and Recognition

The author would like to thank all of those who have helped me in working towards the completion of this thesis. First, I would like to thank my advisor, Dr. Kevin Kochersberger, for his outstanding guidance and support. Dr. Kochersberger is a pleasure to work with and has had a great impact on my academic and professional development; and for this I thank him. I would also like to thank Dr. Jeff Kozak for his support and his continuing efforts to develop the emerging Micro Air Vehicle program at RIT. Also, I am forever grateful for Dave Hathaway's advice, help and guidance when it comes to all things practical.

In addition, I must thank my family and friends for their constant support and encouragement. My family has encouraged me from the beginning; to them I owe a great deal. Also, the friends I have had the pleasure of knowing at school have been both supportive through the difficult times and great fun during the happy times. Finally, and most importantly, I would like to thank my girlfriend Kelly for all her support and understanding. I am extremely grateful for all RIT has given me; most of all for her.

Table of Contents

List of Figures

List of Tables

List of Symbols

a , b , c , d	Length dimensions of load cell balance
AoA , α	Angle of attack
C_L	Lift coefficient (3-D)
C_D	Drag coefficient (3-D)
C_M	Pitching moment coefficient (3-D)
D	Drag
L	Lift
l	Rolling moment
M , *m*	Pitching Moment about quarter-chord
n	Yawing moment
Q	Dynamic pressure of freestream
Re	Reynolds number
S	Wing reference area
S	Side force
u	Uncertainty of a subscripted quantity
U_∞	Free-stream velocity
$x_{1\text{-}4}$	Load cell designations
subscript R	Raw load value, before calibration matrix
subscript L	Load actually applied, after calibration matrix

1 Introduction

Over the past decade the study of Micro Air Vehicles (MAVs) has generated increasing interest in the field of aerospace due to their potential military, intelligence and civilian applications. As the miniaturization of electronic sensor and surveillance equipment continues the list of possible mission profiles for very small, limited-duration aircraft grows. Video surveillance, chemical/biological agent detection, forest-fire observation and highway traffic monitoring are among the numerous envisioned uses. The advantages of using MAVs for these applications include the ease of transport and operation by a single individual, the low-cost of MAVs in comparison to other technologies, the difficulty in counter-detection of MAVs in a hostile environment, and the ability to gather real-time information without endangering human lives.

Experimental data gathered for use in full-scale aircraft design at Reynolds numbers greater than 10^6 is readily available. Low Reynolds number research for MAV scale aircraft is much more scarce. As defined by the Defense Advanced Research Projects Agency, an MAV is an aircraft with a maximum linear dimension of less than 15 centimeters [1]. By this definition, most MAVs have an operating Reynolds number between 50,000 and 200,000 [2]. While the library of aerodynamic knowledge at these low Reynolds numbers inherent to MAV applications is steadily growing, much work remains. Facilities with the ability to gather accurate experimental data on the performance of MAVs will be in a position to truly lead the way in this emerging area of aerospace design.

Current, state-of-the-art fixed-wing MAV designs range in size from four to eight inches, with a variety of onboard electronics. In general, total gross weights of these designs range from 50 to 150 grams [3]. Of course, the aerodynamic forces acting on MAVs are

proportional to the size and weight of the aircraft themselves. To gather meaningful experimental data, the measuring system must be capable of resolving gram-size forces.

1.1 Existing Balance Options

A preliminary investigation into the balance systems available for use in the Rochester Institute of Technology (RIT) Subsonic Wind Tunnel was conducted. Two noteworthy options exist: a computer integrated, six degree of freedom sting balance and a simple student designed mechanical balance. Their suitability for use in MAV testing was determined.

1.1.1 NK Mini-6 Sensor Model II

The most technologically advanced balance system available in the RIT Wind Tunnel is the NK Mini-6 Sensor (Figure 1-1). This balance is a standard internal 6 degree of freedom sting balance design. It is computer integrated and results are captured and displayed via manufacturer provided software.

Figure 1-1 NK Mini-6 Sensor, Model II

The NK Mini-6 Sensor has primarily been utilized in the past to obtain 2-D aerodynamic data from large airfoils. Some graduate and undergraduate [4] work has been

performed using the NK Mini-6, with varying degrees of success. The load ranges and specifications for the balance are seen in Table 1-1.

Forces	Drag	+/- 50 lb
	Lift	+/- 50 lb
	Side	+/- 50 lb
Moments	Pitch	+/- 75 in-lb
	Yaw	+/- 75 in-lb
	Roll	+/- 25 in-lb

Table 1-1 NK Mini-6 Sensor Load Specifcations

Using standard uncertainties of 0.2% of full-scale, Table 1-2 shows the expected uncertainties in the measurements.

		Uncertainties	
Forces	Drag	+/- 0.1 lb	+/- 45.4 g
	Lift	+/- 0.1 lb	+/- 45.4 g
	Side	+/- 0.1 lb	+/- 45.4 g
Moments	Pitch	+/- 0.15 in-lb	+/- 68.0 g-in
	Yaw	+/- 0.15 in-lb	+/- 68.0 g-in
	Roll	+/- 0.05 lb	+/- 22.7 g-in

Table 1-2 NK Mini-6 Force Uncertainties

Taking lift as the primary example, the predicted 45 gram uncertainty in an expected MAV lift measurement of perhaps 100 grams total is unacceptable. This, coupled with the fragility of the system, its sometimes difficulty in use, and extreme expense of repairing has forced the conclusion both in this and prior work [5] that this balance system cannot be used with MAV scale models.

1.1.2 Low Reynolds Number Small-Model Mechanical Balance

A thesis completed in late 2003 by Abe [6] constructed a set of two mechanical balances capable of excellent resolution in determining loads on very small airfoils. Abe tested small airfoils (9cm and 6.75cm span) for lift and drag at a Reynolds number of approximately

5,500. Another balance was used to test the same airfoils for pitching moment at a Reynolds number of 40,000 and rolling moment at 6,800. Resolution results were excellent, and were on the order of ±0.02 grams for lift and drag.

The lift and drag force balance is based on a simple knife-edge pendulum system. Lift and drag measurements may be statically determined by performing a moment analysis about the knife-edge axis. This balance design is shown in Figure 1-2. A more detailed description of the balance and its operation is detailed in Section 4.

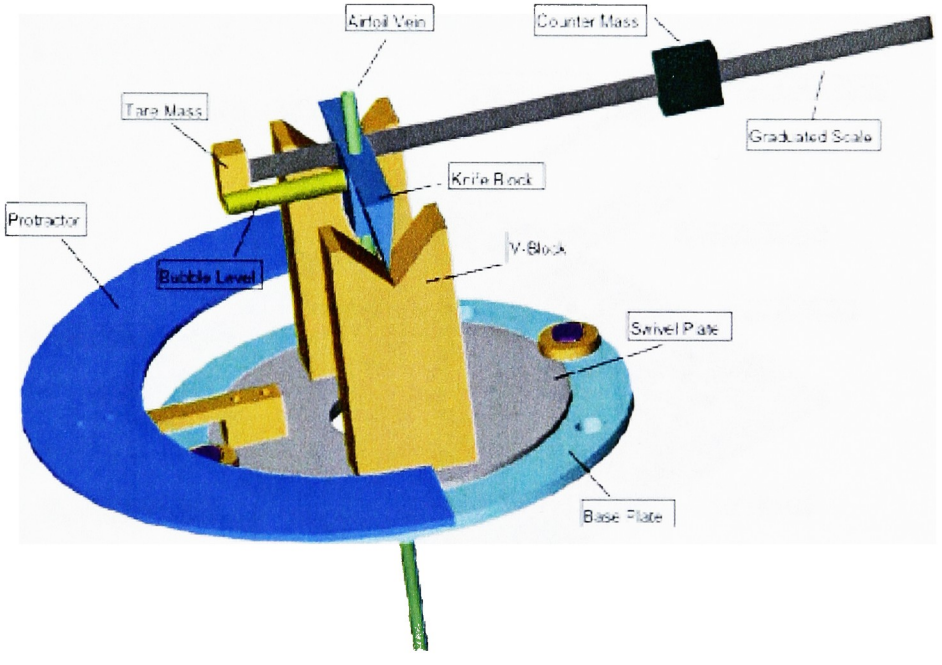

Figure 1-2 Knife Edge Mechanical Force Balance [6]

During the initial testing performed with this balance using an MAV scale model (8 x 8 inch flat plate) the balance performed well. However, it was soon shown that at higher loads the knife edge block lifts from the V-support blocks. During testing in either the lift or drag configurations, when the aerodynamic load increases beyond approximately 50 grams, the

knife edge lifts from the support and the balance becomes unusable. Before this break-point, however, the balance showed excellent results and repeatability. It was concluded that with several modifications this force balance system could be improved and made fully functional for MAV testing. Unfortunately, preliminary work with the pitching and rolling moment balance created by Abe, Figure 1-3, determined it to be impractical for use with the larger MAV models to be studied. The complex series of rods and linkages would have been too bulky and unfeasible. Modifications to this moment balance were briefly considered, but abandoned in favor of concentration on a modified force balance design.

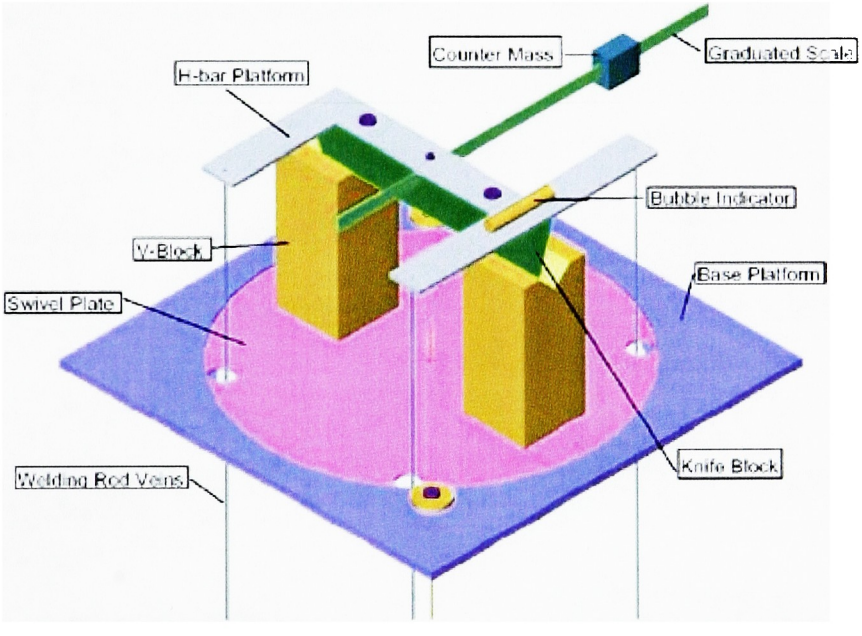

Figure 1-3 Knife Edge Mechanical Moment Balance [6]

1.2 *The RIT Subsonic Wind Tunnel Facility*

Given the proper balance system, Rochester Institute of Technology's Closed Circuit Subsonic Wind Tunnel can be an ideal facility for the experimental testing of MAV scale models. Figure 1-4 shows a schematic of the wind tunnel.

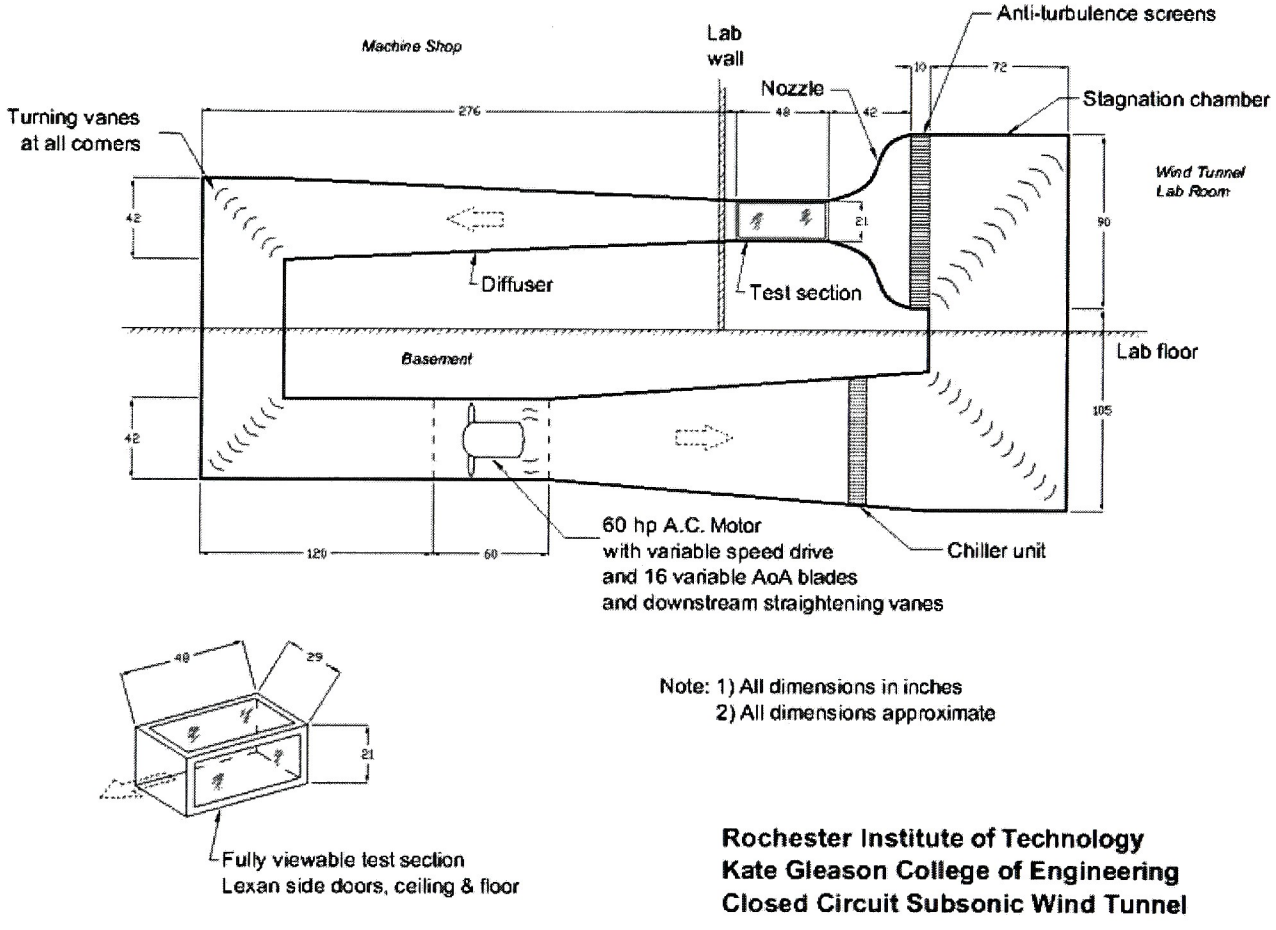

Figure 1-4 RIT Closed Circuit Subsonic Wind Tunnel

The 29 x 21 x 48 inch test section is suitably sized for testing MAVs; with careful positioning of the balance and model wall effects can be minimized. After a recent test-section redesign, all four sides of the test section are completely accessible and viewable. The wind tunnel is powered by a 60 horsepower variable speed motor and has 16 variable angle

of attack fan blades. These blades can be adjusted between a high-pitch and a low-pitch setting and gives the wind tunnel an approximate sustained test section speed range of between 6 m/s and 55 m/s (20 – 180 ft/s). Turning vanes, straightening vanes and anti-turbulence screens positioned strategically within the tunnel serve to improve flow quality within the test-section. Also, a student-designed chiller unit serves to correct the temperature stability problems inherent in closed circuit tunnel designs. The unit provides a stable temperature of ±0.5 degrees Fahrenheit within the test section.

Additionally, a three-dimensional motorized traversing system is available for accurate positioning of sensors within the test section. Mounted above the test section, this traverse is generally utilized to position pitot tubes and other flow sensors. A variety of pressure transducers, pitot-static tubes and a hot-wire anemometer system are also available for use. Finally, a dedicated National Instruments computer data acquisition system is also accessible.

1.3 Statement of Problem and Scope

From the very beginning, the general goal of this thesis has been to develop the RIT Subsonic Wind Tunnel's capabilities to the point where it can provide meaningful, accurate and publishable experimental data to the emerging Micro Air Vehicle Program at RIT. The initial examination of the current capabilities of available balances and the tunnel facility itself described above showed the areas in need of attention. Prioritizing the needs, it was decided that the acquisition or fabrication of a balance system designed specifically for the small loads of MAVs was the most important first step. The other needs, as outlined in Section 8, are not absolutely necessary to the gathering of meaningful experimental data and were considered secondary.

The acquisition of a sting balance system similar to the NK Mini-6, but with the necessary MAV scale load ranges, was briefly considered. The lowest price quoted from all the manufacturers contacted was well beyond current capital available to the wind tunnel for equipment purchases through grants and internal funding.

Due to the above considerations, the primary objective of this thesis is the design, fabrication and testing of a balance system for the RIT Wind Tunnel capable of measuring longitudinal forces (lift, drag and pitching moment) on MAV scale models. Two balances are created by this research. First, several simple modifications to the Low Reynolds Number balance created by Abe are made. These modifications allow the balance to capture lift and drag beyond the 50 gram limit imposed on the previous design. Other changes made increase the usability and accuracy of the system and are based on suggestions made by Abe. A simplified testing regime is performed with the new mechanical balance to show its usefulness and validity in testing MAVs.

Secondly, an entirely new balance system is designed and fabricated. Furthermore, several key factors were included in the development of the design:

- Balance shall be suitable to both a student-laboratory setting and a graduate research environment (robust, straight-forward, user-friendly, yet accurate)
- Balance and experimental setup should utilize previously available equipment whenever possible
- Automation and computer integration to be used whenever possible (to start the process of fully automating experimental runs into LabVIEW)
- Total cost should be kept to a minimum (< $3,000)

To this end, all components of the balance not commercially purchased were designed to be student-machined in the RIT Machine Shop. This both kept costs down and ensured that the balance is easily repaired.

Following the design and fabrication of the balance, the system is tested, validated, and uncertainty and repeatability determined. Comparison versus published results helps confirm the accuracy of the system. Finally, testing of the 2003-2004 RIT Micro Air Vehicle, *Thnikkaman*, is performed to show the balance's applicability to testing an actual, full-scale Micro Air Vehicle.

2 Literature Review

A voluminous amount of experimental research has been done at Reynolds numbers greater than 10^6. Based on this data, accurate analytical and computational methods of determining aerodynamic performance have been developed. Conversely, far less work has been done in the Reynolds number region of interest to Micro Air Vehicles. Figure 2-1 illustrates these Reynolds numbers in comparison to that of other aircraft.

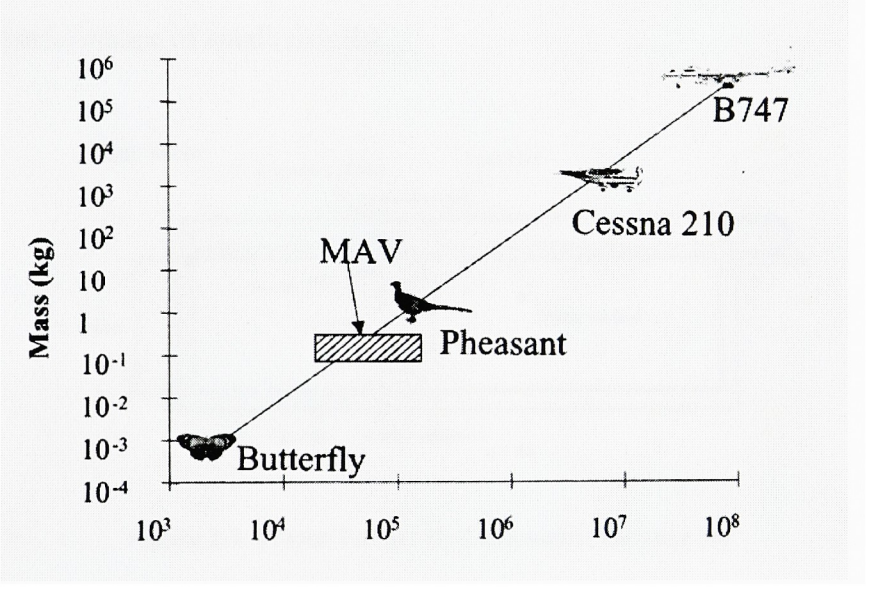

Figure 2-1 Size comparison of aircraft by Reynolds number [2]

Over the past ten years, as interest in MAVs has grown, balances have been specifically designed for use in testing MAV scale models. A review of several characteristic balances designed to measure very small forces follows.

2.1 Laitone & Sunada

Work by Laitone [7] utilized a two-component beam balance with a sensitivity of ±0.01g. This balance allowed the accurate measurement of both lift and drag of small models to a Reynolds number as low as 10^4.

Very low Reynolds number airfoil testing has often been accomplished via water tunnels. Sunada et al [8] performed finite wing testing using a typical water tunnel setup. Their setup, seen in Figure 2-2, used a ceiling mounted load cell to determine the 3-D aerodynamic performance of small airfoils.

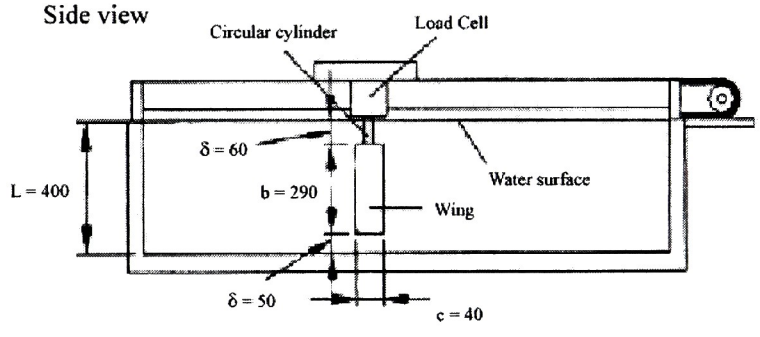

Figure 2-2 Water Tunnel Hydrodynamic Balance [8]

2.2 UND-FB2 Longitudinal Balance

Recent MAV research at the University of Notre Dame has used both a water tunnel and an open-circuit low speed wind tunnel. A single ceiling mounted external balance design, Figure 2-3, is used with both [9].

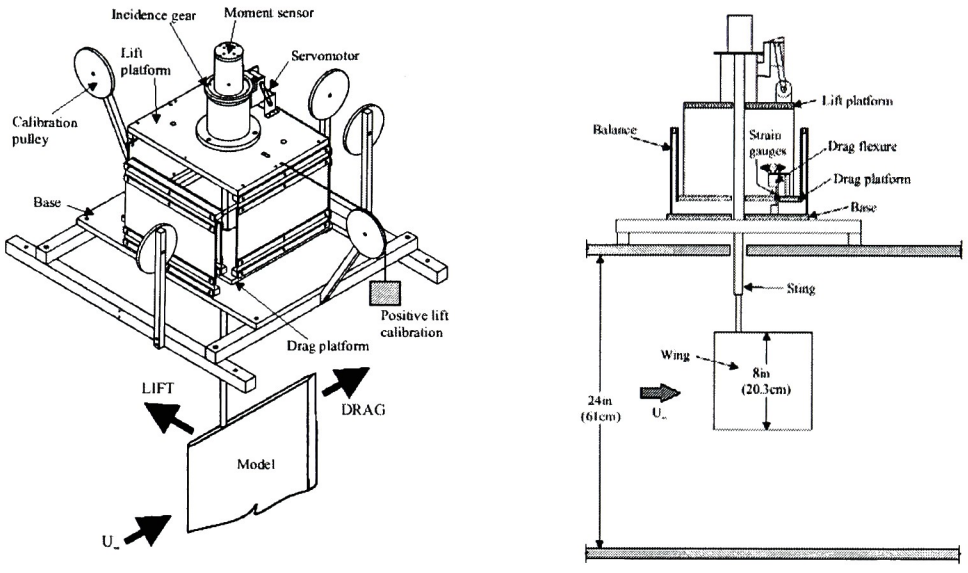

Figure 2-3 Notre Dame Experimental Balance UND-FB2 [9]

In this balance, model forces are transmitted through the sting to the external platform. Flexures then isolate the force components and two sets of thin foil strain gages measure the force in the lift and drag direction. A commercially available moment sensor mounted to the top of the sting measures pitching moment directly. Data acquisition and signal conditioning is accomplished via National Instruments software (LabVIEW) and hardware. Calibration is done using a series of strategically positioned pulleys and dead weight. The weight applies a known force in a specific direction to the balance platform. Finally, the angle of attack of the model is controlled through a computer integrated servomotor and gear system. The motor can accurately advance the gear and achieves an uncertainty in angle of attack of 0.5-0.7 degrees [15].

The main sources of uncertainty in the Notre Dame balance were determined to be the quantization error of the data acquisition card and the uncertainty of the strain gage output

voltage. In the end, the average uncertainty in C_L and C_D measurements using this balance was determined to be on the order of 6%.

2.3 Internal Sting Balances

Among the most popular balance systems in use in aerodynamic research are fully enclosed, internal sting balances. These balances can be designed to measure any combination of the six degrees of freedom and have a variety of load ranges. Internal sting balances operate on the same principles as external balances except the necessary components are very small and enclosed within a cylindrical housing. The balance is mounted onto or, often, inside the model. Flexures and strain gage bridges determine the forces and moments in each direction. Calibration of complex six degree of freedom balances is critical. From calibration, a cross-sensitivity matrix is determined and is used to determine the final values of forces and moments. Many such balances are available commercially (Figure 2-4), but are often prohibitively expensive to those without significant financial support.

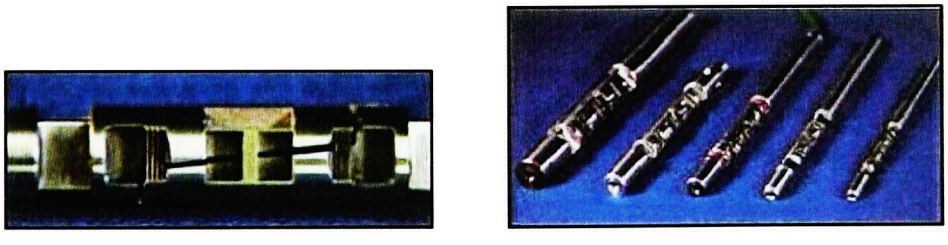

Figure 2-4 Several Internal Sting Balances available from AeroLab Inc. [10]

3 Design Concepts of Balances

A wind tunnel balance is fundamentally a system that directly measures the actual forces and moments on models in a wind tunnel test section [11]. These forces are then used to determine the aerodynamic performance of full-scale aircraft in flight. Uniquely, when dealing with such small aircraft as MAVs, the full aircraft itself can often be tested in the wind tunnel, negating concerns of scaling and modeling errors.

Wind tunnel balances fall into two general categories: internal and external. Depending on the anticipated experiments, balances can be designed to measure any or all of the six degrees of freedom associated with flight. The large majority of both internal and external balances utilize strain gages. Both types usually operate on similar principles of flexures and links; although internal balances must have all the necessary transducers and mechanical elements tightly packaged in a very small volume (Figure 3-1).

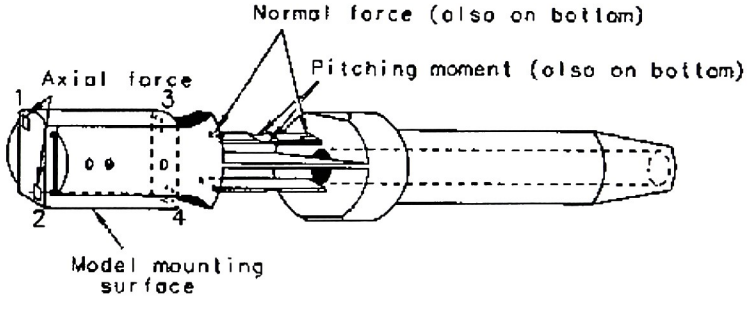

Figure 3-1 Internal strain gage balance design [11]

Internal balances can also be time-consuming and troublesome to calibrate because of large interactions between the degrees of freedom.

Most external balances in use today can themselves be divided into several subgroups: platform, yoke and pyramidal. These types are so-named because of their primary load carrying members. Although slightly different in design, all external balances operate on

the same basic principles. From the test model, a support ("sting") attaches to the balance apparatus. The balance consists of a number of flexures and pivoting linkages that allow only force in a certain direction to be transmitted to various supporting members. By measuring the force transmitted through these members, usually via strain gages, the aerodynamic loads on the model can be determined. Figure 3-2 shows a basic layout for a six DOF platform balance and the lettered forces that must be measured.

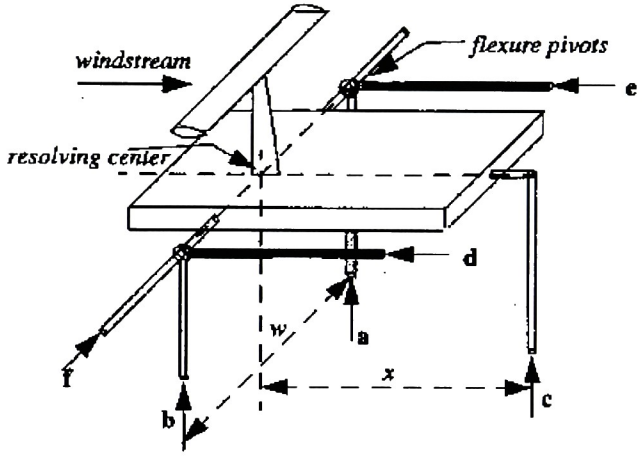

Figure 3-2 Schematic layout of a simple platform external balance [11]

The forces and moments are then determined through simple statics:

$$L = -(a+b+c) \qquad D = d+e \qquad S = -f$$

$$l = (a-b)(0.5w) \qquad n = (e-d)(0.5w) \qquad m = cx$$

While the above setup and simple equations should work in theory, all balances require a great deal of calibration and adjustment before they read properly. Many different sources of error impact the balance and can cause direct errors or cross-sensitivities in the readings. These include deflections in the mounting and balance system itself, friction in balance linkages and pivots, and errors in the readings of the transducers. To nullify these concerns, a proper and accurate calibration procedure must be performed.

4 Design and Modification of Mechanical Force Balance

As described in detail by Abe [6], the RIT Low Reynolds Number Mechanical Balance operates on a simple pendulum system whereby the aerodynamic forces on the model are counteracted by a weight applied to a slide-rule above the pivot point. Figure 4-1 shows the balance in the lift configuration. On the left, the balance is in equilibrium. On the right, a load is applied by the wind and the balance swings out of equilibrium. By applying a small weight to the green moment arm, the balance can be brought back into equilibrium and the lift force determined.

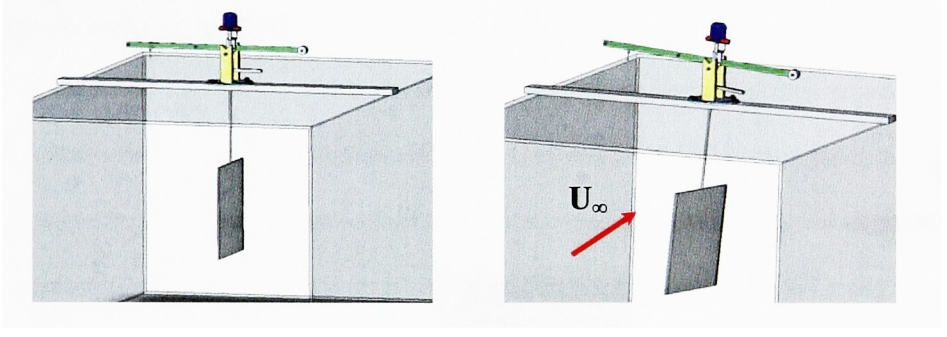

Figure 4-1 Modified mechanical balance in lift configuration

By rotating the entire system 90 degrees via a rotating base plate, drag can be measured in a similar fashion. Using calibrated weights and an accurate measurement system, the lift force or drag force can be determined through a simple static analysis. Figure 4-2 shows the forces acting on the balance and the distances necessary for this analysis. This diagram depicts the drag configuration.

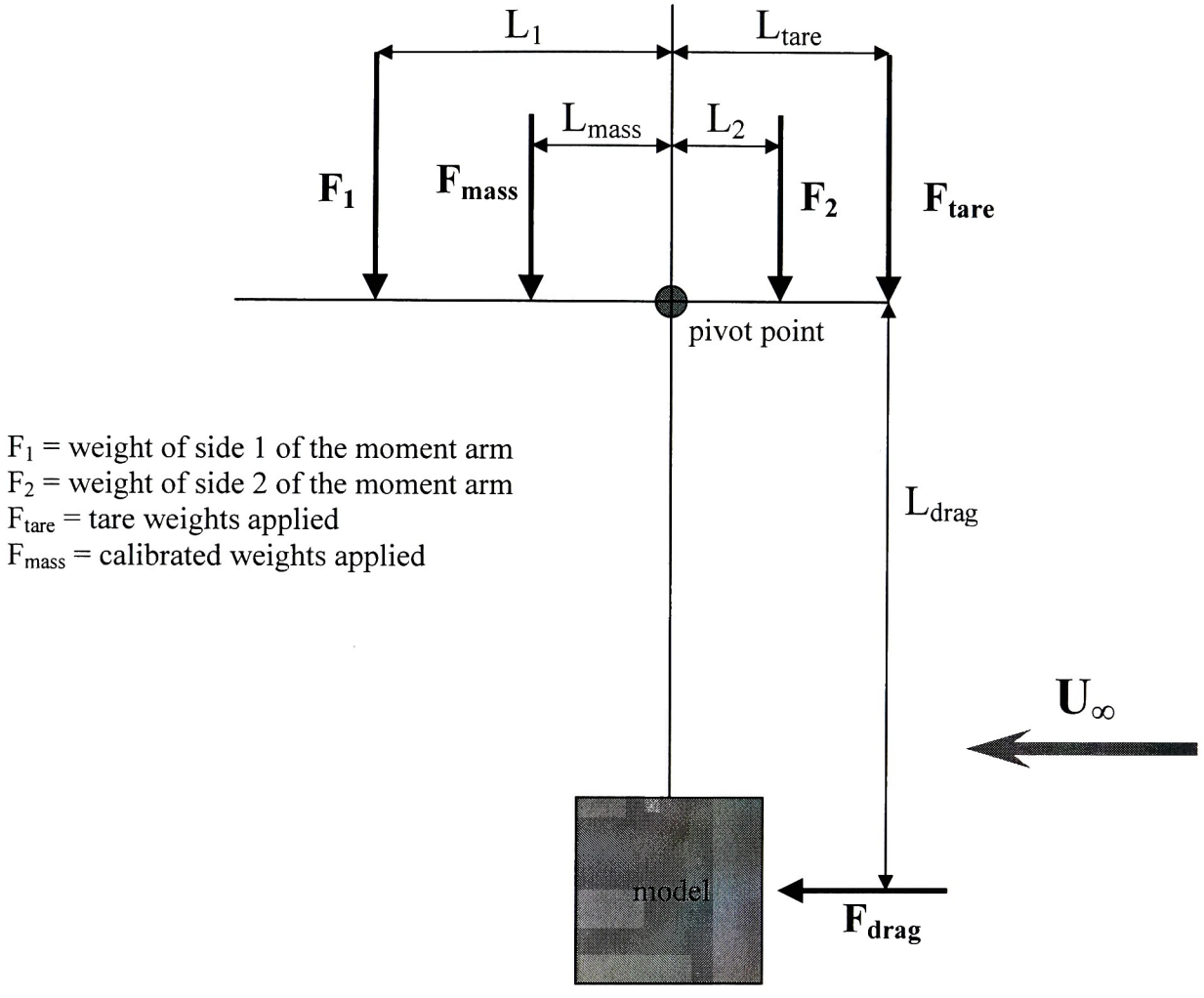

Figure 4-2 Force diagram of Mechanical Balance in drag configuration

Summing the moments about the pivot point shown in Figure 4-2, the result for the drag force is shown in Equation 4-1.

$$F_{drag} = \frac{F_1 L_1 + F_{mass} L_{mass} - F_2 L_2 - F_{tare} L_{tare}}{L_{drag}}$$

Equation 4-1

If properly tared using small weights at the location of F_{tare}, the above equation reduces to Equation 4-2.

$$F_{drag} = \frac{F_{mass} L_{mass}}{L_{drag}}$$

Equation 4-2

Therefore, the aerodynamic force on the model can be reduced to a function of only the mass on the slider, the distance from the pivot to the slider and the length of the sting arm from pivot to model. The benefit of this balance lies in its simplicity. The author has found with experience that when dealing with the very small forces encountered in MAV experiments, simple is sometimes better and electronics and automation can be more hindrance than help. The lift configuration is assumed by rotating the swivel plate 90 degrees, such that the pendulum swings in the lift direction. The determination of the lift force is similarly accomplished as in the above equations.

With the design proven to be accurate at very small loads, the process of updating the system for use with MAVs was begun. Several modifications were made. The first, and most important, design change is the modification of the pivot itself. The previous design relied on a knife edge to provide a nearly frictionless pivot. The weight of the model and balance apparatus was used to hold the knife edge down onto the support blocks. As described previously, a problem occurs at higher loads when the knife edge lifts off from the supports. Adding extra weight to the knife edge block did not help an appreciable amount and only served to decrease the resolution of the device as a whole. The solution used was to change the pivot from a knife edge to a shaft and bearing arrangement. Miniature ABEC-5 ball bearings are embedded in the upright support blocks and a precision ground steel shaft used

as the central pivot. This eliminated the possibility of the apparatus lifting from the design point while keeping a nearly frictionless pivot action.

With the major issue hindering the use of the mechanical balance with MAVs solved, secondary modifications were made to increase the accuracy and reliability of the measurements. These consisted of:

- An electronic protractor mounted to the very top of the system. This provided a digital readout of the angle of attack of the model accurate to within +/-0.2 degrees and did away with the cumbersome and inaccurate method of measuring the angle by hand.
- A laser level to allow for more accurate determination of equilibrium position. Initially installed in part for earlier work, this modified laser pointer projects a beam to the opposite end of the room. With a small dot placed on the wall, the balance operator can more accurately determine precise equilibrium compared to the previous bubble level.
- Improvements were also made to the moment arm and sliding mass. Extension of the moment arm allows for larger loads to be measured more easily. A slider fashioned from aluminum and fitted snugly over the 1/64 inch division slide rule replaces the filament string previously used to hang weights. This makes for easier, more accurate and less time consuming experiment runs.

These modifications and the basic operation of the balance itself are illustrated in Figure 4-3. A small calibration procedure was performed to the modified balance to confirm its accuracy. Using a small pulley loads were applied to the sting arm in the lift and drag

directions. The results were as expected and the balance read less than 1.0% deviation from the applied loads.

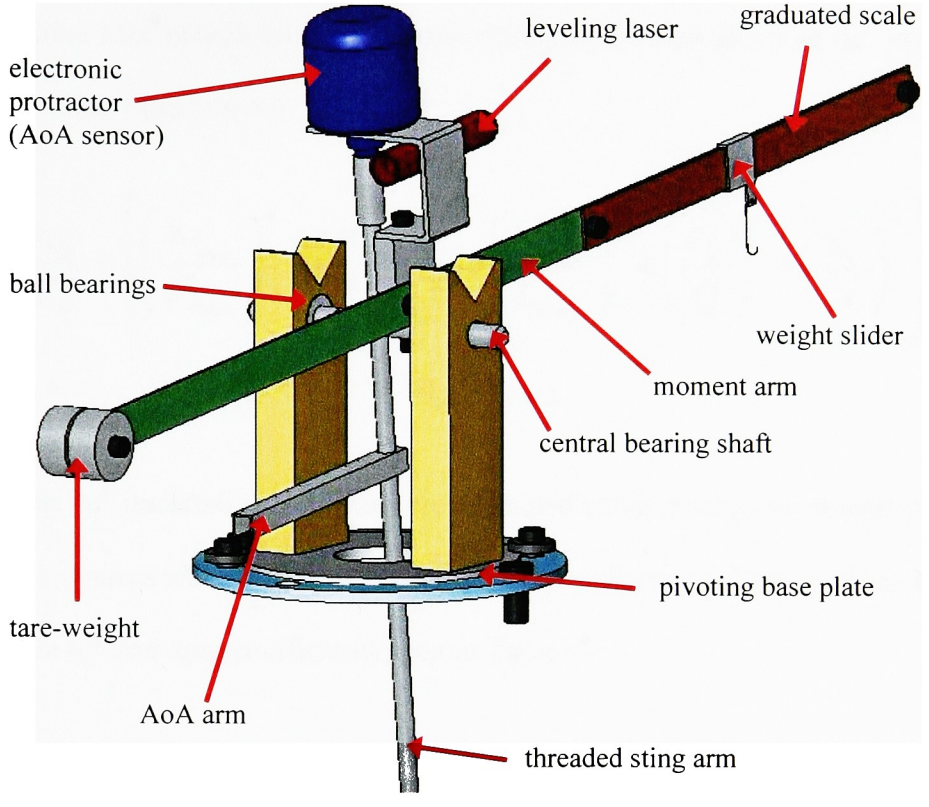

Figure 4-3 Modified mechanical balance

4.1 Expected Uncertainty of Mechanical Balance

While the fundamental balance design proved successful in prior testing, a rudimentary uncertainty analysis was performed to estimate the expected uncertainty in the measurements acquired by the balance. As used by Torres and Mueller [15], and shown in detail by Abe, a standard Kline-McClintock uncertainty analysis was calculated. This method incorporates the uncertainties in all necessary measurements; including lengths, mass, and pressure. From Equation 4-2, the drag coefficient is calculated via Equation 4-3.

$$C_D = \frac{F_{mass} L_{mass}}{L_{drag} QS}$$

Equation 4-3

Using the Kline-McClintock method, the uncertainty in the calculation of the drag coefficient is evaluated using Equation 4-4.

$$\frac{u_{C_D}}{C_D} = \left[\left(\frac{u_{F_{mass}}}{F_{mass}} \right)^2 + \left(\frac{u_{L_{mass}}}{L_{mass}} \right)^2 + \left(\frac{u_{L_{drag}}}{L_{drag}} \right)^2 + \left(\frac{u_Q}{Q} \right)^2 + \left(\frac{u_S}{S} \right)^2 \right]^{\frac{1}{2}}$$

Equation 4-4

From this, the "u" uncertainty quantities are estimated using measurement least counts, machining tolerances and manufacturers' supplied specifications. This results in the uncertainty in lift and drag coefficients seen in Table 4-1.

$\frac{u_{C_D}}{C_D} = \frac{u_{C_L}}{C_L} \approx 1.06\%$
$u_{C_L} = u_{C_D} = \pm 0.01$

Table 4-1 Expected Uncertainties for Mechanical Balance

5 Design of Load Cell Balance

Although the update and modification of the simple mechanical balance previously designed at RIT was a goal of this project, a more important aspect of the research is the design and implementation of an entirely new balance system. Several limitations exist concerning the mechanical balance (discussed further in Section 8) even in its modified form, and a new system that answers these concerns is designed. The design of this balance is a radical departure from the mechanical balance in that it is rigid system capable of measuring all longitudinal degrees of freedom simultaneously using computer-integrated load cells.

5.1 Reference / Coordinate Systems

Reference frames are very important to the study of aerodynamics, and several of them exist. In wind tunnel testing, three reference systems are of the most importance: tunnel, wind and body. A standard assumption is often made (and is made for this research) that the wind and tunnel references are identical. This assumption stipulates that the relative velocity in the wind tunnel test section is in-line and parallel to the test section itself. A diagram of the tunnel/wind coordinate system can be seen in Figure 5-1.

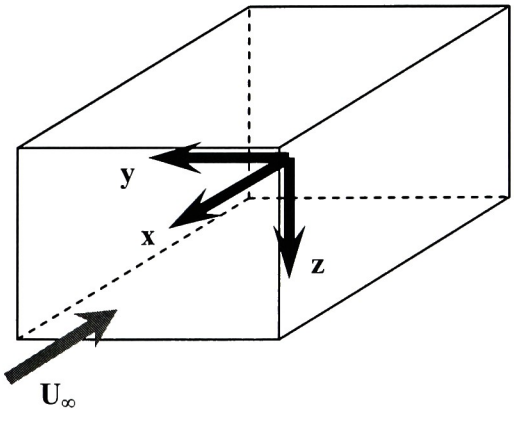

Figure 5-1 Tunnel / Wind reference system

The body reference system is "attached" to the model body. Centered at the body's center of mass, this reference system moves as the body itself is moved. Conversions between the wind system and body system are accomplished through transformation matrices incorporating angle of attack and sideslip angle. These transformations are necessary because some balance systems (particularly internal sting balances) measure forces in the body axes. Aerodynamic forces, on the other hand, are recorded in the wind system. External balances, including the one designed for this research, often measure forces directly in the wind reference system, thereby eliminating the need for this sometimes confusing step.

5.2 Fundamental Design

The basic design for the load cell balance does not neatly fit into any of the standard categories of external balance types described in Section 3. However, it most closely resembles a platform balance in that it reads the forces on the model via linkages to transducers located beneath the tunnel. The basic design of the balance is in Figure 5-2 on the following page.

A large, heavy and very stable positioning and model support system already existed for use in the tunnel lab. In an effort to utilize this existing hardware and not design a "scratch" system for controlling both AoA and sideslip, the balance design was tailored to incorporate the support system. This system can control model angle of attack and sideslip angle by a pair of hand-cranks. These are being automated for digital control via the use of stepper motors by a complementary thesis. All experiments presented in this research, however, were performed using the traditional hand-crank method.

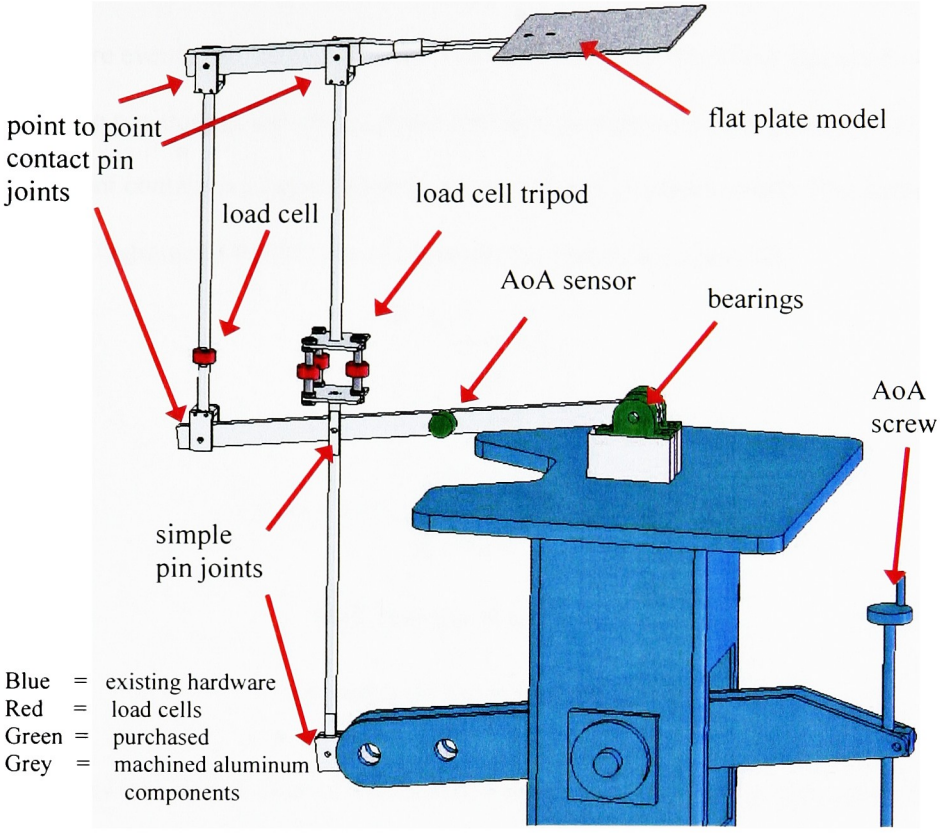

Figure 5-2 Load cell balance

The linkages and rods of the balance all consist of standard 6061, multipurpose aluminum. The strength of aluminum is more than sufficient for the small loads encountered by the balance. Also, the excellent machinability and inexpensive nature of 6061 lend itself to a low-cost, student fabricated device. The central pivot joint atop the support platform is accomplished with commercially available, ½ inch, flange mounted ball bearings. These bearings are placed precisely over the pivot lower in the AoA adjustment mechanism.

The two lower joints in the machined aluminum pieces are simple pin joints. Because these joints are below the load cells, friction in them is inconsequential; they only serve to change the AoA of the setup given input from the hand-crank. The upper joints, however,

need to be as frictionless as possible. Bearings were initially considered for accomplishing this, but were eventually discarded in favor of conical set screws. These set screws allow for more precise positioning and easier alignment than a traditional bearing setup. Also, their point-to-point contact in a larger-angled countersink will provide a nearly frictionless rotation. A diagram of this point-to-point contact is shown in Figure 5-3.

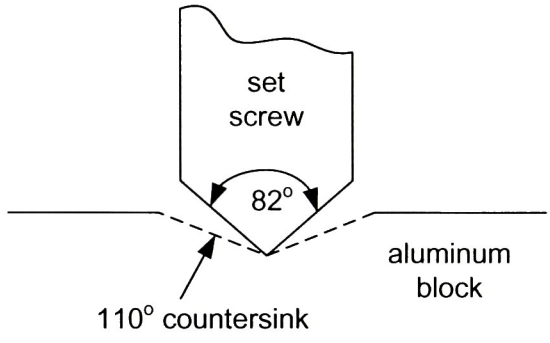

Figure 5-3 Set screw joint arrangement

Figure 5-4 shows another view of the set screw joint (with one aluminum support block removed for clarity). These joints are the three joints in Figure 5-2 described as "point to point contact pin joints".

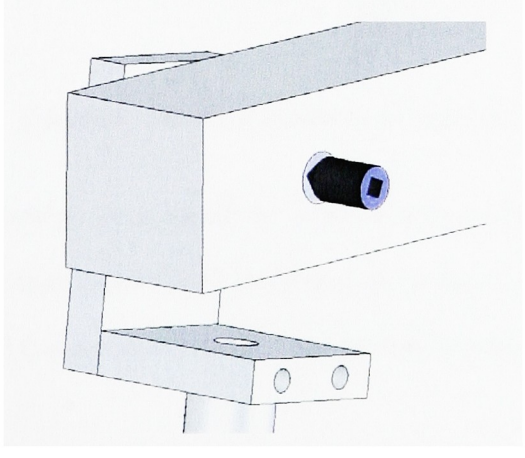

Figure 5-4 Model of a set screw joint

With a set screw on either side of the central sting-arm block, the position of the block within the joint can be easily adjusted by manipulating the set screws. Furthermore, a simple qualitative assessment of the friction of this type of joint showed results that easily matched those of a similar joint constructed using standard ABEC-1 bearings.

A close-up view of the load cell arrangement is seen in Figure 5-5.

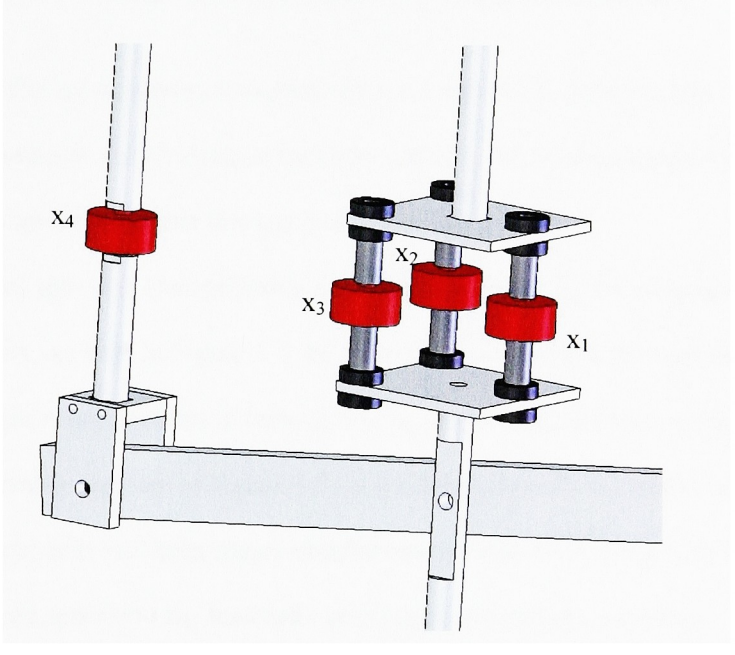

Figure 5-5 Close-up of transducer arrangement

The load cells themselves (seen in red) are commercially purchased from Omega Engineering, Inc. While more expensive than options such as foil strain gages, these Omega LCFA Mini Tension and Compression Load Cells (Figure 5-6) were selected for their ease of use and adaptability.

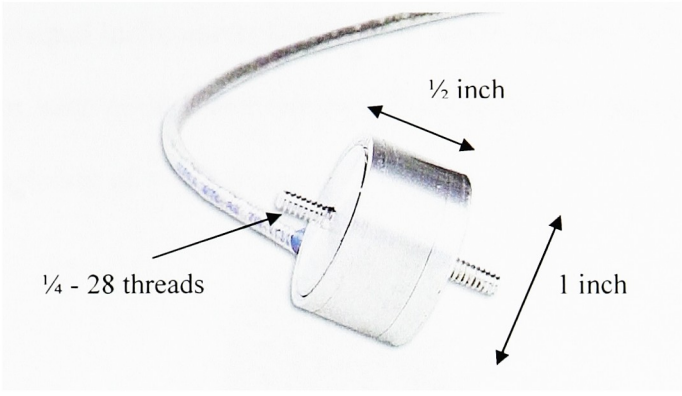

Figure 5-6 Omega LCFA Mini Tension and Compression Load Cell

Because the load cells are a popular commercially available brand, different load ranges can be purchased if necessary. Future experiments may require a higher load range; by simply swapping the replaceable load cells this can be accommodated.

Finally, sets of spherical steel self-aligning washers are used in the integration of the three front load cells. As seen in Figure 5-7, these washers consist of male and female halves. They allow for slight misalignments in threaded connections. Placing these washers (shown in black in the assembly diagram of Figure 5-5) at the connections between the balance linkages and the load cells will help ensure that the load cells see only axial force. Any moment or side force applied to the load cells could cause an erroneous reading.

Figure 5-7 Self-aligning washer set

Finally, an Accustar Electronic Inclinometer is used to detect the angle of attack of the system. This barrel shaped inclinometer (Figure 5-8) can be attached to any vertical, flat portion of the system, such as the lower arm as in Figure 5-2, and reports AoA to a digital readout with an uncertainty of +/-0.1 degrees.

Figure 5-8 Accustar Electronic Inclinometer used for AoA

5.3 *How it works*

As previously mentioned, the designed balance works on the same principles as a platform balance. Force is measured at several key points in the balance apparatus, and equations used to determine the lift, drag and pitching moment on the model. Figure 5-9 is a diagram of the balance's dimensional layout, the location of the load cells and the forces acting upon the model.

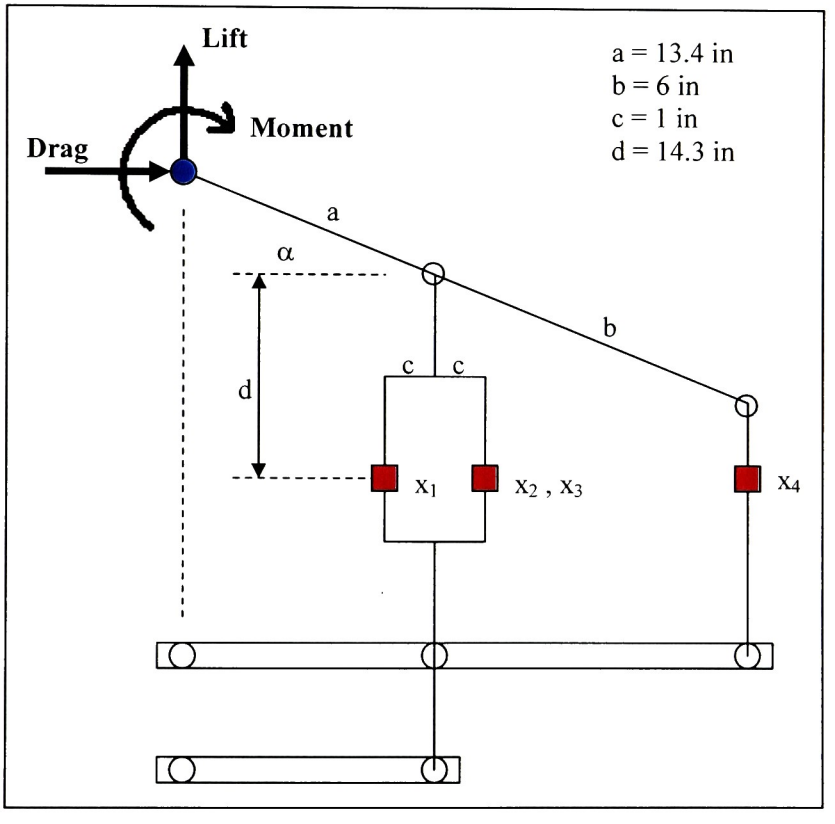

Figure 5-9 Diagram of balance

The key to this design is the "drag tripod". The drag tripod consists of the front three load cells (x_1, x_2 and x_3), laid out in a triangular shape with one in the front and two in the back. This tripod sits below the first upright linkage in the system. This entire upright

connects to the bottom of the apparatus, below the critical tripod, at two pin joints that are vertically in-plane. These two pin joints effectively cantilever the front upright. Also, because the two pin joints are vertically in line with each other, the upright will stay vertical no matter what angle of attack is given to the model. A note must be made that a tripod arrangement itself is not theoretically necessary. Two load cells could be used in place of three and arrive at the same results. This was deemed unrealistic in practice however due to the fragility of such a setup. Two, in-line load cells would be very susceptible to incorrect readings and breakage under even small side loadings. With the tripod arrangement, any side loading is taken by the off-center load cells x_2 and x_3. Only small side loadings are expected in the symmetrical testing to be performed with the balance, and given careful calibration the tripod arrangement will cancel such loadings out of the results. Any small asymmetric loading or misalignment in assembling the balance will also be accounted for by this calibration of the system as a whole. Figure 5-10 shows the tripod configuration.

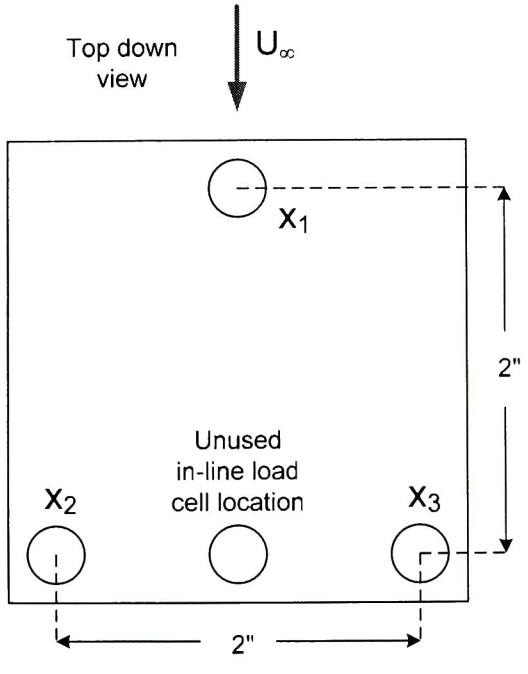

Figure 5-10 Tripod configuration

The rear upright, as seen in Figure 5-9, contains the load cell x_4 and is only pinned at one point below the load cell. This pin joint is one of the special conical set screw joints described earlier. By having only this one, near-frictionless pin joint, the rear upright will not impede force in the drag direction. Therefore, all drag force is taken up by the cantilevered front upright and the drag tripod.

With this in mind, a simple statics analysis using Figure 5-11 and Figure 5-12 can derive the equations for the aerodynamic forces.

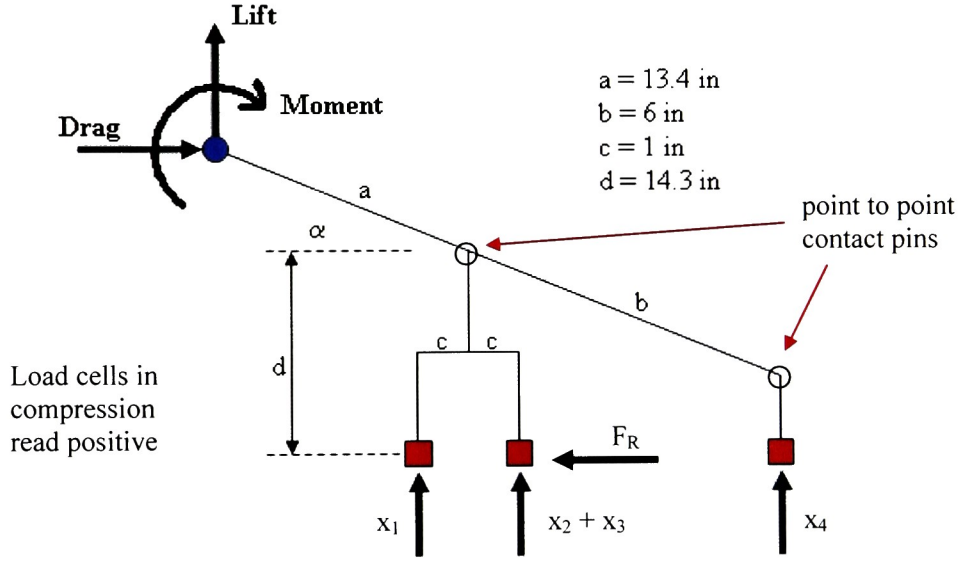

Figure 5-11 Free body diagram of balance

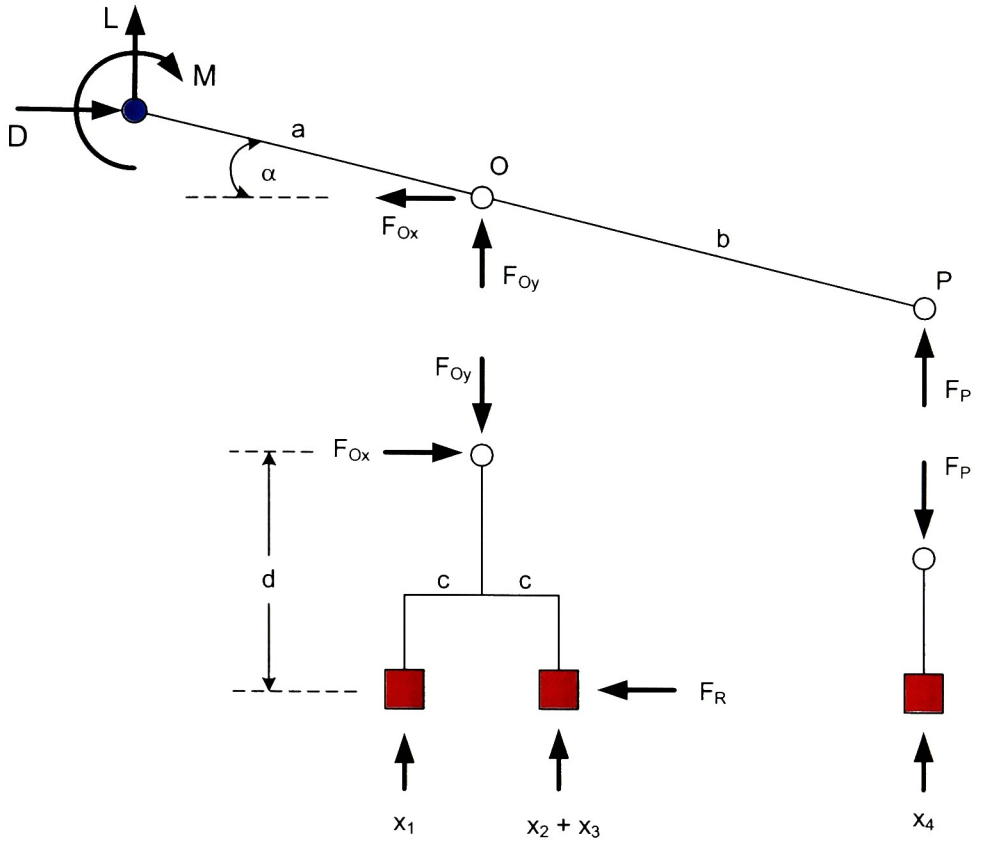

Figure 5-12 Free body diagram of individual components of balance

Lift is the simplest. Because the uprights are always vertical, perpendicular to the airflow, the combination of the readings of all the load cells is the lift force.

$$L = -[x_1 + x_2 + x_3 + x_4]$$

Equation 5-1

Drag force is derived by looking at the moment the cantilevered front upright must exert to counteract the force in the axial direction.

$$D = [x_2 + x_3 - x_1]\frac{c}{d}$$

Equation 5-2

Pitching moment is also dependent on the dimensions of the balance itself.

$$M = \cos\alpha[(x_1 + x_2 + x_3 + x_4)a + x_4 b] - Da\sin\alpha$$

Equation 5-3

Using these three equations and expected load ranges for MAV scale models, an analysis determined the best choice of ranges for the load cells. This showed that the front and rear load cells, x_1 and x_4, will bear a much larger portion of the force transmitted through the balance. Figure 5-13 shows the spreadsheet portion of this analysis. The blue spreadsheet cells are manipulated to determine what the load cells will approximately read under certain loads and given certain balance dimensions.

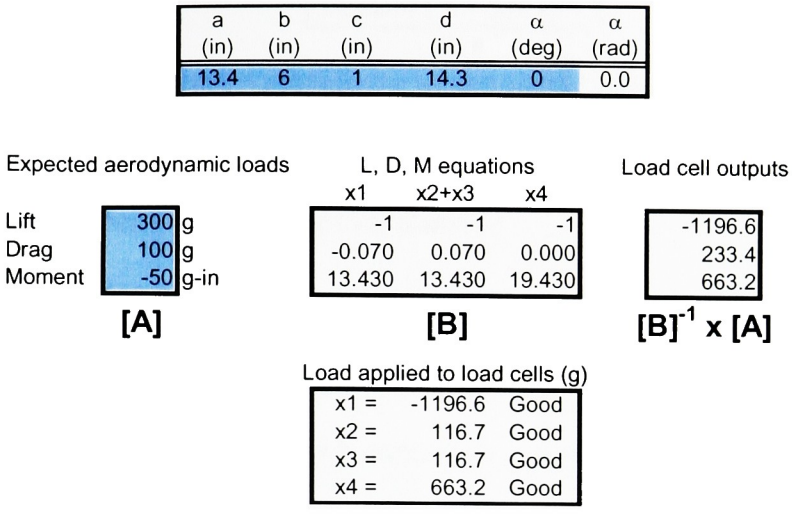

Figure 5-13 Spreadsheet to determine necessary load cell ranges

This method helped determine the results seen in Table 5-1.

x_1	+/- 5 lb
x_2	+/- 1000 g
x_3	+/- 1000 g
x_4	+/- 5 lb

Table 5-1 Selected load cell ranges

These load cell ranges allow for a wide range of testing. As stated previously, the balance can be made to tolerate greater loads by simply swapping the load cells for ones with a greater range. But with the current load cell configuration, the recommended maximum do-not-exceed force values are in Table 5-2. Of course, these are only approximate, and a more accurate way of determining the limits of the balance is to monitor the outputs of the load cells themselves during testing and ensure they do not exceed their limits. This is accomplished through the computer integration of the balance discussed in Section 5.5.

Lift	+/- 500 g
Drag	+/- 200 g
Moment	+/- 500 g-in

Table 5-2 Maximum recommended balance limits

5.4 Expected Uncertainty of Load Cell Balance

Being developed concurrently with the selection of the load cells and dimensional design was a determination of the expected uncertainty of the system. As with the mechanical balance, Kline-McClintock method was used. Applying the differential methods described by Kline-McClintock to the equations for lift, drag and pitching moment results in the uncertainty equations below.

$$u_L = \left[\left(u_{x_1}\right)^2 + \left(u_{x_2}\right)^2 + \left(u_{x_3}\right)^2 + \left(u_{x_4}\right)^2\right]^{\frac{1}{2}}$$

Equation 5-4

$$u_D = \left[\left(\frac{c}{d}u_1\right)^2 + \left(\frac{c}{d}u_2\right)^2 + \left(\frac{c}{d}u_3\right)^2 + \left(\frac{(x_2 + x_3) - x_1}{d}u_c\right)^2 + \left(\frac{c}{d^2}((x_2 + x_3) - x_1)u_d\right)^2\right]^{1/2}$$

Equation 5-5

$$u_M = \left[\begin{array}{l} \left(u_{x_1} a\cos\alpha\right)^2 + \left(u_{x_2} a\cos\alpha\right)^2 + \left(u_{x_3} a\cos\alpha\right)^2 + \left((a+b)u_{x_4}\cos\alpha\right)^2 \\ + \left((x_1 + x_2 + x_3 + x_4)u_a\cos\alpha + Du_a\sin\alpha\right)^2 + \left(x_4 u_b\cos\alpha\right)^2 + \left(u_D a\sin\alpha\right)^2 \\ + \left((x_2 + x_3 - x_1)u_c\right)^2 + \left(u_\alpha\sin\alpha\left[(x_1 + x_2 + x_3 + x_4)a + x_4 b\right] + u_\alpha D\cos\alpha\right)^2 \end{array}\right]^{1/2}$$

Equation 5-6

These equations are easily converted to uncertainty in the coefficients by including the uncertainty in dynamic pressure, chord and span.

5.4.1 Factors Impacting Uncertainty

From the above equations several conclusions can be drawn to minimize the uncertainty of the system. For instance, Equation 5-4 shows that lift uncertainty is entirely dependent on the uncertainty of the load cells. By minimizing the uncertainty in the load cells, lift uncertainty is also minimized. Of course, a compromise must be struck between the needed range of the load cell, the error associated with it and the fragility of the system.

Unlike lift, the uncertainty in drag force can be minimized by carefully choosing the dimensions of the balance itself. It is seen in Equation 5-5 that dimensions "c" and "d" are in many of the right-hand side terms. By minimizing "c" and maximizing "d" the total uncertainty in drag will decrease. This essentially gives a larger moment arm to the drag tripod, resulting in larger forces and greater resolution.

Pitching moment uncertainty is impacted by many factors as shown by the large number of terms in Equation 5-6. No single solution can significantly decrease this uncertainty. The best conclusion is to decrease both dimensions "a" and "b" while also keeping load cell uncertainty to a minimum. Unfortunately, realistic dimensional and design concerns mean "a" and "b" cannot be made very small. Dimension "b", for example, is the distance from the front upright to the model quarter-chord. This cannot be made very small because the model must be located far enough away from the balance so that interference effects are minimal. Because of these concerns, pitching moment uncertainty could be difficult to minimize and may be fairly significant.

5.4.2 Calculating Expected Uncertainty

Table 5-4 on the following page shows the preliminary uncertainty estimates of the forces and moment using data from Selig [12]. This data represents an approximation of the forces that are expected when testing over a portion of the recommended range of the balance. These uncertainties are calculated using the manufacturer's specifications for load cell error and the loose machine tolerances expected from student machining of parts. Several things are of note considering this table:

- By the nature of the method used, *the uncertainty percentage increases dramatically with very low forces/moment values*. Table 5-3 perhaps more realistically illustrates the expected uncertainty in coefficient form throughout the testing range.
- The maximum possible errors in the load cells and tolerances were used to arrive at a large, conservative estimate for the possible uncertainty in the system. Manufacturer calibration sheets and in-house calibration showed much lower uncertainty in the load cells. If these lower values are correct it would significantly decrease the uncertainty in the results, particularly for the highly load cell dependent lift uncertainty.
- Pitching moment uncertainty is, unfortunately, very high. This is due to the variety of factors discussed in the previous section.

Theoretical Uncertainty
C_L = +/- 0.03
C_D = +/- 0.003
C_M = +/- 0.05

Table 5-3 Expected uncertainty in coefficients

Preliminary Kline-McClintock Uncertainty Analysis

u_{x1} (g)	u_{x2} (g)	u_{x3} (g)	u_{x4} (g)	a (in)	$u\alpha$ (in)	b (in)	$u\beta$ (in)	c (in)	$u\chi$ (in)	d (in)	$u\delta$ (in)	α (deg)	$u\alpha$ (deg)
4.5	2	2	4.5	14.3	0.01	6	0.01	1	0.01	14.3	0.01	2	0.5

Approximate uncertainties expected:

AoA	LIFT			DRAG			MOMENT		
(deg)	L (g)	u_L (g)		D (g)	u_D (g)		M (g-in)	u_M (g-in)	
-9.1	-70.1	6.96	9.9%	7.1	0.38	5.3%	37.7	116.0	307.8%
-8.7	-70.1	6.96	9.9%	7.1	0.38	5.3%	35.1	116.1	331.3%
-8.1	-67.5	6.96	10.3%	6.5	0.38	5.8%	21.7	116.3	534.9%
-7.6	-70.5	6.96	9.9%	7.2	0.38	5.2%	17.8	116.5	654.6%
-7.1	-67.5	6.96	10.3%	6.5	0.38	5.8%	-5.0	116.6	2327.8%
-6.6	-67.3	6.96	10.3%	6.5	0.38	5.8%	-14.0	116.7	835.4%
-6.1	-59.2	6.96	11.8%	5.0	0.38	7.5%	-49.8	116.8	234.5%
-5.7	-53.0	6.96	13.1%	4.2	0.37	9.0%	-62.1	116.9	188.3%
-5.1	-41.9	6.96	16.6%	3.2	0.37	11.5%	-85.1	117.0	137.4%
-4.6	-36.0	6.96	19.4%	2.9	0.37	12.7%	-73.1	117.1	160.1%
-4.1	-28.9	6.96	24.1%	2.7	0.37	14.0%	-83.9	117.2	139.6%
-3.6	-21.9	6.96	31.7%	2.5	0.37	14.9%	-71.8	117.2	163.2%
-3.1	-14.8	6.96	46.9%	2.4	0.37	15.7%	-83.9	117.3	139.7%
-2.6	-6.8	6.96	102.9%	2.3	0.37	16.3%	-74.9	117.4	156.8%
-2.1	1.5	6.96	469.0%	2.2	0.37	16.7%	-88.2	117.4	133.2%
-1.6	10.4	6.96	67.0%	2.2	0.37	17.0%	-79.6	117.4	147.5%
-1.1	19.5	6.96	35.8%	2.2	0.37	17.2%	-88.3	117.5	133.0%
-0.5	36.1	6.96	19.3%	2.2	0.37	17.3%	-92.0	117.5	127.7%
0.0	50.7	6.96	13.7%	2.2	0.37	17.0%	-104.8	117.5	112.1%
0.5	62.4	6.96	11.2%	2.3	0.37	16.4%	-107.3	117.5	109.5%
1.1	76.4	6.96	9.1%	2.4	0.37	15.5%	-111.4	117.5	105.5%
1.5	81.0	6.96	8.6%	2.4	0.37	15.3%	-108.7	117.5	108.0%
2.0	90.4	6.96	7.7%	2.5	0.37	14.7%	-107.0	117.4	109.7%
2.5	96.4	6.96	7.2%	2.6	0.37	14.4%	-96.9	117.4	121.2%
3.1	104.1	6.96	6.7%	2.6	0.37	14.1%	-94.2	117.3	124.5%
3.6	111.4	6.96	6.3%	2.7	0.37	13.8%	-84.3	117.3	139.0%
4.1	119.5	6.96	5.8%	2.8	0.37	13.5%	-84.5	117.2	138.8%
4.6	127.4	6.96	5.5%	2.8	0.37	13.2%	-77.0	117.1	152.2%
5.1	135.5	6.96	5.1%	2.9	0.37	12.7%	-76.6	117.1	152.9%
5.7	144.9	6.96	4.8%	3.1	0.37	11.9%	-67.2	116.9	174.0%
6.1	152.5	6.96	4.6%	3.4	0.37	10.8%	-69.2	116.9	168.9%
6.7	160.2	6.96	4.3%	3.9	0.37	9.5%	-61.7	116.7	189.3%
7.2	168.0	6.96	4.1%	4.7	0.37	7.9%	-62.6	116.6	186.3%
7.7	173.6	6.96	4.0%	5.6	0.38	6.7%	-54.0	116.5	215.6%
8.2	180.2	6.96	3.9%	6.9	0.38	5.5%	-54.7	116.4	212.8%
8.6	184.5	6.96	3.8%	8.0	0.38	4.8%	-49.4	116.2	235.2%
9.2	192.2	6.96	3.6%	10.6	0.39	3.6%	-47.0	116.0	246.7%
9.8	195.2	6.96	3.6%	11.9	0.39	3.3%	-39.9	115.9	290.2%
10.3	199.3	6.96	3.5%	13.9	0.40	2.8%	-38.1	115.7	303.8%
10.7	201.0	6.96	3.5%	14.9	0.40	2.7%	-32.3	115.5	357.9%
11.3	205.3	6.96	3.4%	17.5	0.41	2.3%	-30.7	115.3	375.5%
11.8	208.1	6.96	3.3%	19.5	0.42	2.2%	-25.4	115.1	452.5%
12.2	209.9	6.96	3.3%	20.9	0.43	2.0%	-25.8	114.9	444.9%
12.8	211.0	6.96	3.3%	21.8	0.43	2.0%	-31.9	114.7	359.6%
13.3	210.9	6.96	3.3%	21.7	0.43	2.0%	-20.8	114.4	549.7%

Table 5-4 Preliminary Kline-McClintock analysis using SD7030 airfoil data [12]

5.5 LabVIEW Integration

In an effort to simplify use of the balance and make the overall system user-friendly, National Instruments LabVIEW 6.0 was used to integrate all the components and serve as an interface between balance and operator. Several National Instruments data acquisition setups are available to the Mechanical Engineering Department, with one dedicated to the Wind Tunnel Lab. These rolling carts offer a variety of instrumentation and acquisition options. For the designed balance, it was necessary to simultaneously capture and process data from the following devices:

- All four (4) load cells
- One (1) K-type thermocouple
- One (1) MKS Baratron 10 torr differential pressure transducer

All of these instruments have millivolt scale output and are ideally suited to be input to LabVIEW through the TC-2095 data acquisition block available in the lab. The line of yellow connectors in Figure 5-14 are shown connected to the TC-2095 at the top of the DAQ panel. The load cells are excited using a hardwired 5V output from the power supply atop the panel.

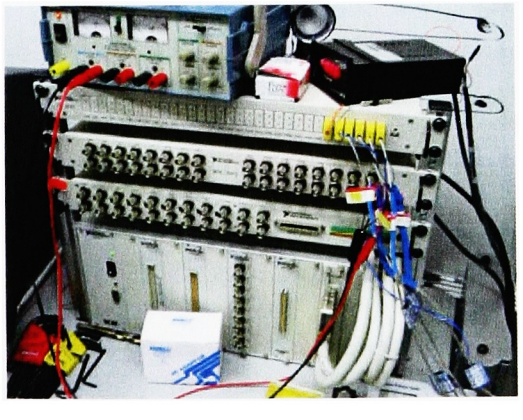

Figure 5-14 Data acquisition panel and setup

The Graphical User Interface (GUI) shown on the next page was developed to make collection of data easier on the user. An extension to the interface and the underlying block diagram itself provide a means for in-depth manipulation of the experiment controls if needed. The block diagram is detailed in Appendix A.

The dual-monitor setup of the LabVIEW computer system used in the lab allows a great deal of information to be presented to the user and is the reason for the elongated nature of the GUI. The GUI is setup in a straightforward manner to reduce the possibility of errors by unfamiliar users. User inputs necessary before an experiment can begin are presented on the upper left, nearest to the default "run" button of all LabVIEW Virtual Instruments. The inputs, shown as boxes with the default white background, are the ambient pressure, model reference area and model reference length. Below these are the optional user inputs. These include the sampling rate parameters and the low-pass filter characteristics. It is expected that most users would leave the selected defaults. These defaults were chosen through experience with the balance and filter design analysis. An analysis using MATLAB 6.1's Filter Design and Analysis Tool determined an order of 6 and a cutoff frequency of 0.5Hz for the low-pass filter characteristics. This low cut-off frequency would ensure most noise would be filtered from the desired DC output signals of the load cells. The characteristics also forced a longer sampling time to be used, but it was found that a somewhat long sampling time gave more precise results anyway.

Following this in the natural progression from left to right are the output readings for ambient temperature and dynamic pressure. The user can select the instruments to be used if necessary by the drop-down boxes; but most users will undoubtedly use the defaults.

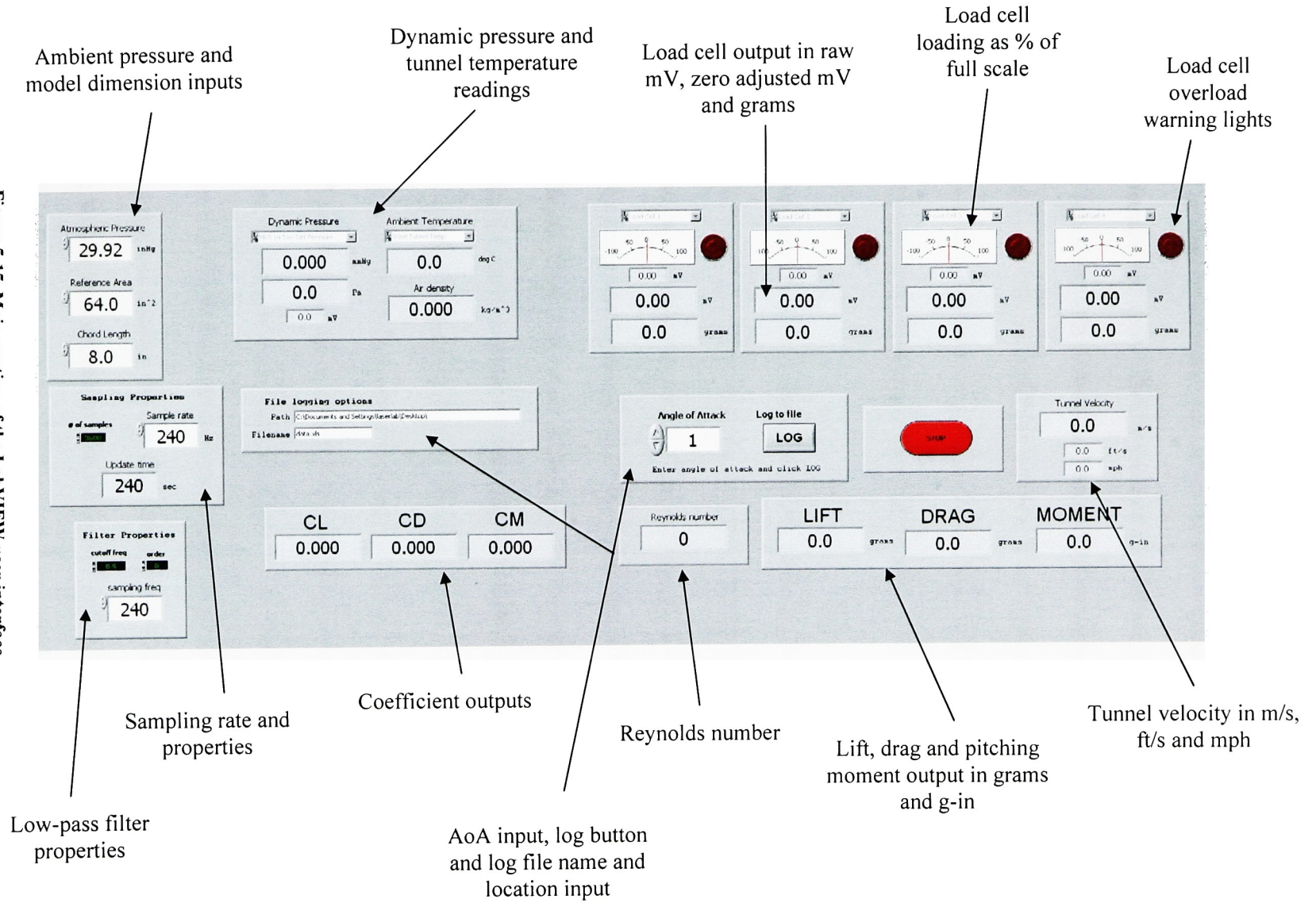

Figure 5-15 Main portion of the LabVIEW user interface

Below the temperature and pressure outputs are user inputs for the name and location of the file to log data to. The data defaults to a tab-delimited Excel spreadsheet file located on the Windows Desktop named "data.xls". Below these text boxes are the coefficient readings from the balance while in action. This is the final piece of information located on the left hand monitor of the computer. It is intended that the user, after inputting all the preliminary information described above at the beginning of the experiment, will focus the majority of the attention during the experiment at the right hand monitor (the one closest to the experiment apparatus itself).

The top of the right-hand monitor features the information on the individual load cells. This includes the user-selectable instrument name, the meter monitoring percentage of full-scale load the transducer is experiencing, an overload warning light to signal when maximum load is being neared for a particular load cell, and output readings of the load cell in millivolts and grams. Below these four boxes is the area that the user will use most frequently. This includes a numerical input for the angle of attack of the system, the button that will log one cycle of data, the red stop-button for stopping the Virtual Instrument (VI), and outputs of tunnel velocity in several units of measure. Finally, below this are the outputs of calculated Reynolds number and the output of lift, drag and pitching moment.

The VI is designed so that it will zero on the initial run. In other words, the VI must be started using the default LabVIEW run button, then stopped using the red STOP button within the VI. This first run will display the raw data and will save the zeroing offsets. On subsequent runs of the VI, the zero offsets will be subtracted from the raw data and the correct zeroed outputs will be displayed and logged. This is described in further detail in Section 6.2, Experimental Procedure.

This balance and its computer interface is the first step in a larger effort to integrate the capabilities of the entire lab and run all experiments automatically through LabVIEW. It is expected that with future projects all the instrumentation and controls necessary for wind tunnel experiments will be controlled via the computer. Indeed, with the automation of only the angle of attack mechanism and tunnel speed controller this longitudinal balance would be fully automated and able to perform "set it and forget it" [13] style runs with minimal real-time operator inputs. Future work recommendations such as this are discussed in Section 8. A photo of the entire experimental setup is shown in Figure 5-16.

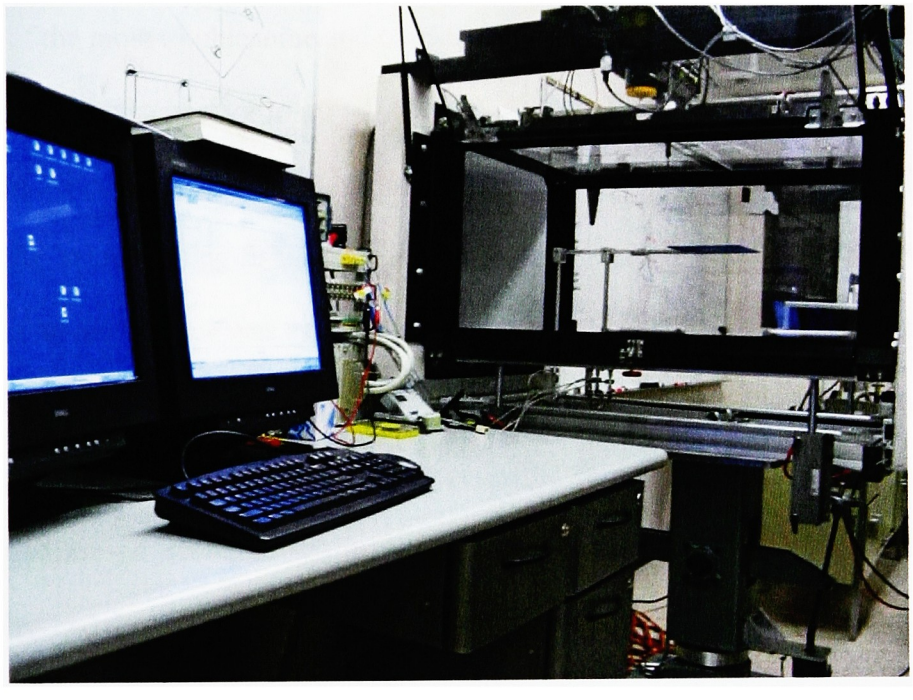

Figure 5-16 Experiment setup

6 Balance Calibration and Experimental Procedure

The experimental setup and procedure for the modified mechanical balance has changed very little from that described by Abe [6] for the original balance. The modifications made to improve the balance and make it ready for use on MAV models did not change the basic functionality. Rather than reiterate that procedure, the interested reader is referred to the previous work for the detailed methods. This section will instead focus on the calibration, setup and experimental methods of the new load cell balance.

6.1 Calibration

One of the most troublesome and time-consuming aspects of any new balance is the calibration of the system prior to initial use [11]. This was also the case in the installation of this balance. After fabrication and assembly of the balance, small calibrated weights were applied to the balance using fishing line and pulleys. It was determined through initial calibration that the balance was extremely sensitive to side-loading. Small amounts of side force, applied at the top of the balance at the model, created a large moment in the roll direction on the drag tripod. This moment was unequally distributed to the three load cells in the tripod and caused erroneous results, particularly in lift. To correct this, the balance was disassembled and the tripod calibrated independently to rid it of sensitivity to side loads.

To do this, the tripod was secured in a vertical position and a "calibration plate" attached to the bottom. Shown in Figure 6-1, this plate consisted of a set of eight small holes drilled concentrically in a circle with a radius of two inches. The plate was attached at the center to the tripod. By hanging small weights from these off-center holes, both lift and side load would be applied to the tripod.

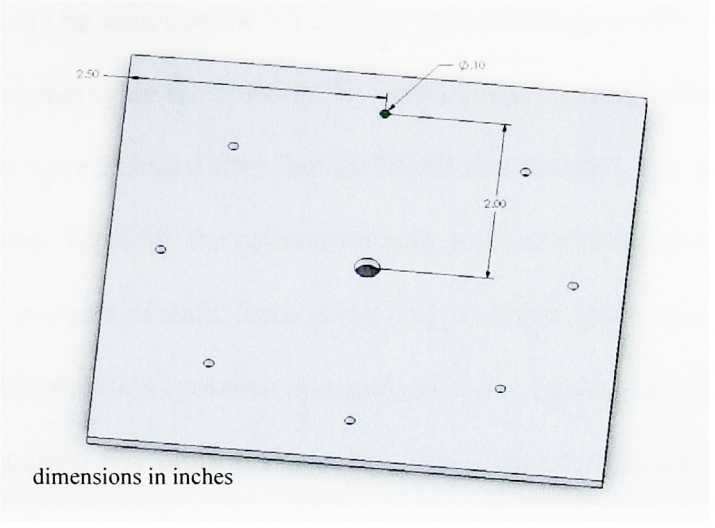

Figure 6-1 Tripod calibration plate

Figure 6-2 shows the results of the tripod calibration. The lateral and longitudinal positions of the holes are shown on the bottom axes (as black points) and the lift output reading when 100 grams of lift is applied at that location is shown on the vertical.

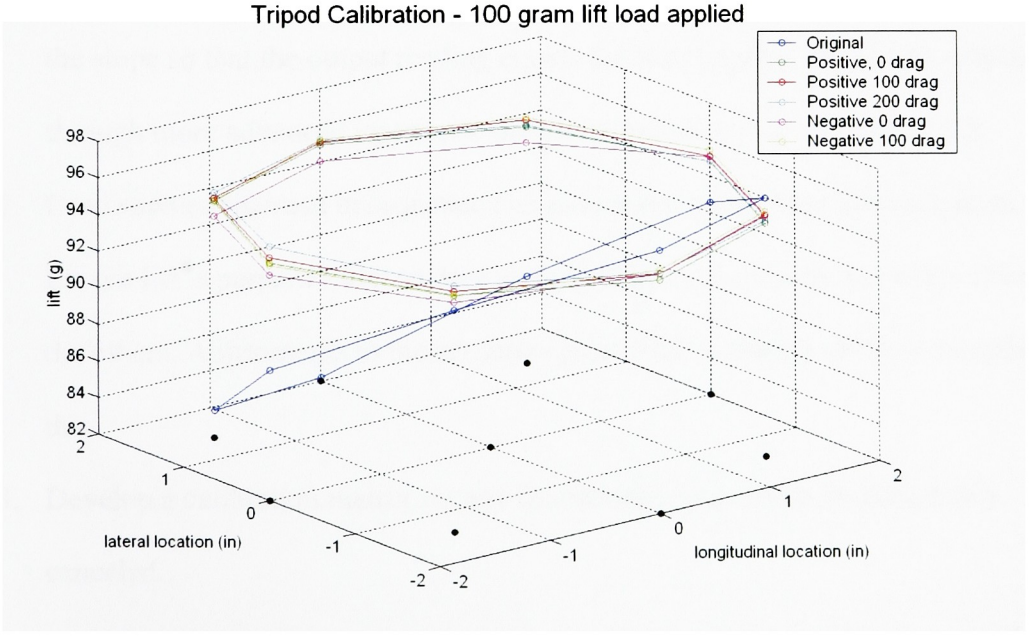

Figure 6-2 Side load calibration of tripod

The blue line in Figure 6-2 shows the original lift output at the points around the calibration plate. It can be seen that the lift reading varies from approximately 98 grams to as little as 82 grams depending on the position. To correct this, the scaling factors of the individual load cells were changed such that the tripod as a system reads the correct lift regardless of side load. To verify the calibration both positive and negative lift were applied, as well as different amounts of static force in the drag direction. The same 100 gram force was applied in the lift direction (positive or negative) under these conditions. The resulting data forms the subsequent five plots in Figure 6-2. They show that the calibrated tripod reads the same lift force within 2 grams regardless of the side load applied.

With the tripod calibrated to cancel side loads, the balance was reassembled and the full system calibrated in a method that is essentially a modified version of the calibration procedure described by Barlow [11]. This method was as follows:

1. Load each component individually (lift, drag and pitching moment), and adjust the slope so that the output reading equals the load applied. This is accomplished through more advanced inputs not shown in the main GUI of Figure 5-15.
2. Load each component in sequence and reduce the interactions between them. Ensure lift is perpendicular to drag and pitching moment does not affect either of the others. Adjustments to the set screw joints can be made to help accomplish this.
3. Develop a calibration matrix for any interactions that cannot be completely canceled.
4. Repeat loadings and combined loadings to determine repeatability and validity of the calibration.

The calibration matrix is determined by loading the components individually and recording the outputs of all three results. Assumptions of linearity and proper zeros are made. For instance, the lift read, L_R, is approximated as the linear combination of the lift load applied, the drag load applied and the pitching moment load applied (L_L, D_L, M_L). This can be expressed as in Equation 6-1.

$$L_R = K_{11}L_L + K_{12}D_L + K_{13}M_L$$

Equation 6-1

These expressions are then gathered in matrix form as Equation 6-2.

$$K = \begin{bmatrix} \frac{L_R}{L_L} & \frac{L_R}{D_L} & \frac{L_R}{M_L} \\ \frac{D_R}{L_L} & \frac{D_R}{D_L} & \frac{D_R}{M_L} \\ \frac{M_R}{L_L} & \frac{M_R}{D_L} & \frac{M_R}{M_L} \end{bmatrix}$$

Equation 6-2

Ideally, this K matrix would be a simple identity matrix. But the interaction between the components makes at least some of the other terms non-zero.

By inverting the K calibration matrix and multiplying by the vector of the "read" or "raw" values, the actual applied loads are determined (Equation 6-3).

$$\begin{bmatrix} L_L \\ D_L \\ M_L \end{bmatrix} = [K]^{-1} \begin{bmatrix} L_R \\ D_R \\ M_R \end{bmatrix}$$

Equation 6-3

6.2 *Experimental Procedure and Analysis*

Two methods of conducting experiments with the load cell balance have been developed; the "run" method and the "discrete" method. The latter consists of taking data points individually by setting the desired angle of attack, zeroing the system, turning the tunnel on, logging the data point, and turning the tunnel off. This process is then repeated for the desired number of data sets at that angle of attack before proceeding to other angles. This process can be extremely time-consuming, but has been found to be more accurate and repeatable than the alternative "run" method. The run method involves zeroing the system, turning the tunnel on, and running through the desired angle of attack sweep while pausing to take the necessary data at the needed angles. The primary reason the run method suffers in accuracy compared to the discrete is the run method must take into account changes in the output results due to the balance AoA positioning. When the balance is run through an angle of attack sweep with the tunnel turned off, the output lift, drag and pitching moment will vary a small amount due only to the shifting center of mass of the balance and model. These changes must be accounted for in post-processing and can be difficult to accurately quantify.

Both of these methods require the subtraction of tare values during post-processing. The balance system cannot take into account, in real-time, the drag, lift and pitching moment on the balance apparatus that protrudes into the test section. These tare values must be quantified by performing runs with no model attached to the balance. These tare values are then subtracted from the values obtained by runs with the model attached to determine the forces and moment on the model alone. While not ideal [11], this method of canceling tare forces has been applied to data by many researchers.

Usually, post-processing would also incorporate correction factors for the variety of errors (wake blockage, streamline curvature, boundary effects, etc) inherent in wind tunnel testing. Because no formal correction scheme has ever been developed for the RIT Wind Tunnel, all results presented in this research remain uncorrected. These corrections would most likely be small in nature and would not seriously impact any of the data.

The analysis of all data taken for this research follows a simplified version of the procedures laid out in AIAA standard S-071A-1999, "Assessment of Experimental Uncertainty with Application to Wind Tunnel Testing" [14]. As laid out in the standard, the data set is first examined for identification and elimination of outliers through the use of Chauvenet's Criterion. This involves the determination of a factor δ_k for each data point by finding the absolute value of the difference between that data point and the mean of the set (Equation 6-4).

$$\delta_k = \left| X_k - \bar{X} \right|$$

Equation 6-4

If this factor then meets the requirement shown by Equation 6-5, it is considered an outlier and is rejected from the data set. S_x is the standard deviation of the set and τ is determined from Table 6-1.

$$\delta_k \geq \tau \, S_x$$

Equation 6-5

N	τ
6	1.73
8	1.87
10	1.96
15	2.13
20	2.24
25	2.33

Table 6-1 Chauvenet's criterion

With outliers discarded, the precision error (P_r) of the sample is determined by the standard deviation of the set multiplied by a confidence factor (Equation 6-6). With a large sample size (> 20), a K factor of 2 is generally used.

$$P_r = K S_r$$

Equation 6-6

Bias error is more subjective, and can be extremely difficult to quantify accurately. Bias error consists of error associated with imprecise calibration, calibration against a non-ideal standard and any error that offsets the entire data set from the actual, accurate result. This research quantifies bias error by examining the hysteresis of the system. The hysteresis observed when taking measurements, coupled with a factor to account for calibration errors, becomes the bias error estimate B_r. The total uncertainty, U_r, is then determined from Equation 6-7.

$$U_r = \left(B_r^{\,2} + P_r^{\,2}\right)^{\frac{1}{2}}$$

Equation 6-7

7 Results

A series of experiments was performed to test the balances. The resulting data was compared to published data to confirm validity. The largest study was performed using a flat plate and compared to results published by Torres [15]. All plots presented in this section are reprinted in Appendix B in larger format for clarity.

7.1 Flat Plate

An eight inch square flat plate model, very similar to that used by Torres, was constructed for testing. The plate had a slightly larger thickness-to-chord ratio of 2.6%, but had similar 5 to 1 elliptical leading and trailing edges. The dimensions of the plate are seen in Figure 7-1.

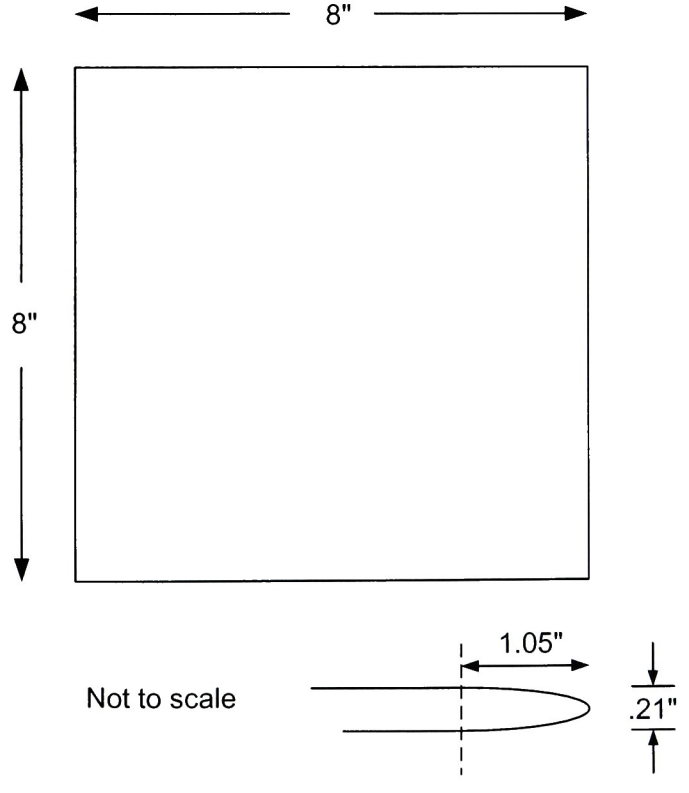

Figure 7-1 Schematic of flat plate model used

7.1.1 Lift

The flat plate was tested on both the modified mechanical balance and the load cell balance. Both methods of using the load cell balance, as described in Section 6.2, were tested. Figure 7-2 is a plot of the results for C_L. Comparing to the published data by Torres, it is seen that all of the data follows the same linear trend with similar slopes. The discrete method, expected to be more accurate than the run method, very closely matches the published data and the results from the mechanical balance. At lower angles of attack, these results correspond very closely, generally within 5%.

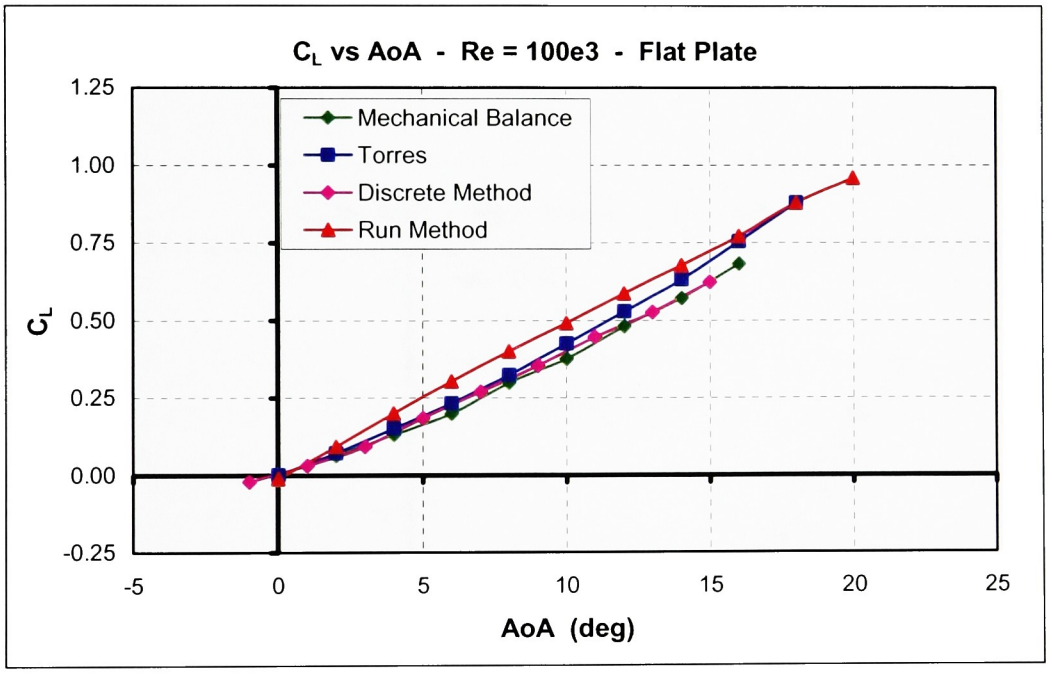

Figure 7-2 C_L vs AoA for flat plate

The largest discrepancy between the run method and the published results occurs at an angle of attack of eight degrees. At this point, the values disagree by approximately 25% or a C_L of 0.08. Because of this, the discrete method is considered a more accurate way of collecting

data, while the run method is acceptable for determining approximate values with larger uncertainty.

7.1.2 Drag

Figure 7-3 shows the results for the coefficient of drag. Once again, all results show the same trends as the comparison data. With drag, however, the results are much closer to the Torres data. Both the run method and discrete method with the load cell balance are generally within a value of 0.01 or 5%. At lower AoA this percentage can increase somewhat due to the low values of C_D. At higher AoA, however, the load cell balance compares excellently with Torres.

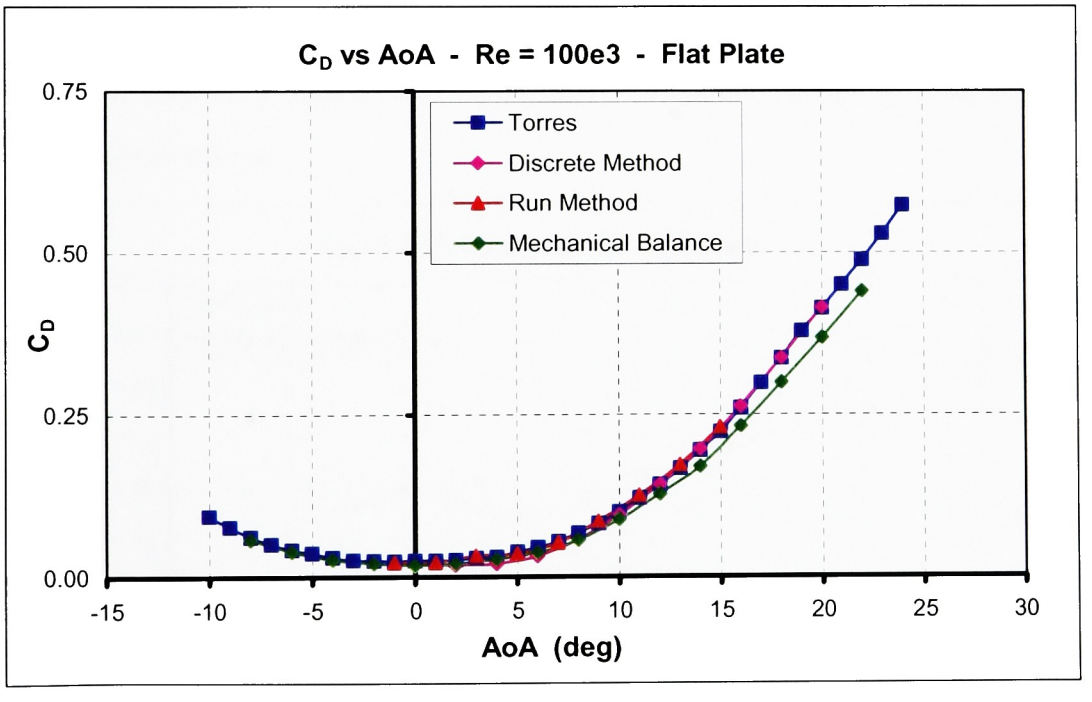

Figure 7-3 C_D vs AoA for flat plate

The mechanical balance also compares very well at lower angles. At angles greater than ten, however, the mechanical balance deviates from the other plots significantly. The cause for this is unknown. However, by the nature of the mechanical balance the model is situated in a different portion of the test section compared to the load cell balance. This difference, or an unknown factor with the balance itself, could lead to this discrepancy at higher angles.

7.1.3 Pitching Moment

Despite a great deal of reconfiguring, testing and analyzing, acceptable results for pitching moment could not be determined. From the preliminary uncertainty analysis presented in Section 5.4, it was known before testing began that pitching moment would be difficult to accurately resolve using the load cell balance as currently designed. Unfortunately it was found that pitching moment could not even be determined to within the large uncertainty bounds generated by this analysis. Figure 7-4 shows a typical result from one run of the load cell balance.

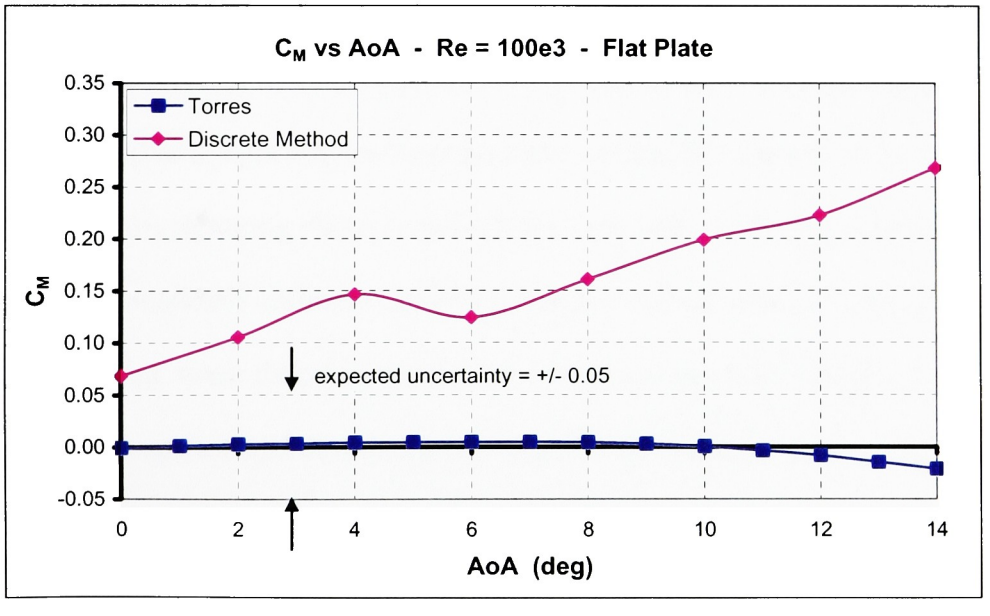

Figure 7-4 C_M vs AoA for flat plate

Pitching moment results from the balance showed a somewhat random, though steadily increasing pattern as AoA increases. This is in contrast to published data that shows a near-zero, gentle upward then downward trend.

The exact cause of the inability to capture moment accurately is unknown, but likely causes can be theorized. The two reasons deemed most likely by the author are improper data processing of tare moment and interference of the balance on the model. Tare processing involves the subtraction of the tare moment determined without the model from the total moment when the model is attached. These numbers are one to two orders of magnitude larger than the resulting difference. This subtraction of two large numbers to arrive at a small number is inherently error prone if the original numbers are even slightly in doubt. The balance itself may also be causing interference errors with the model and the moment output. By further isolating the balance from the model (by an effective shroud, or even better: moving the entire apparatus out of the tunnel such that the model alone is in the freestream), moment errors will be decreased. Although time constraints do not allow these causes to be investigated in the current research, Section 8: Conclusions and Recommendations, details potential solutions to the pitching moment problem that can be explored by future work.

The problems capturing pitching moment are especially troublesome because the balance can be completely calibrated, pitching moment and all, using the procedure outline in Section 6.1. Indeed, when the pitching moment component is loaded independently (by applying weights upward and downward the same distance from the quarter-chord) very little interaction on lift and drag are seen. Despite this, because the balance otherwise works as predicted theoretically, and the same theory shows the balance capable of capturing pitching

moment, it is surmised that future work will determine (and correct) the actual cause of the pitching moment problems.

7.1.4 Experimental Uncertainty

Using the methods described in Section 6.2, the uncertainty in the experimental results is estimated. Precision error is dependent exclusively on the standard deviation of the data gathered at each individual angle of attack. The scatter of data gathered from the load cell balance using the discrete method of data collection is shown in Figure 7-5.

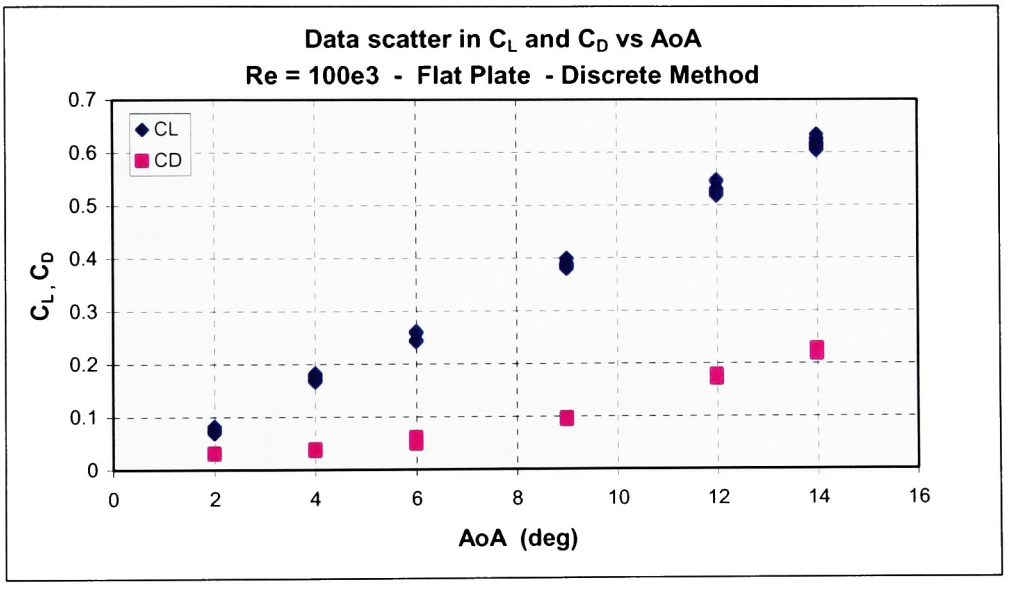

Figure 7-5 Data scatter from 10 runs used to estimate precision error

Bias error is more subjective and is estimated using hysteresis. During experiments utilizing the discrete method the hysteresis was measured and plotted in Figure 7-6.

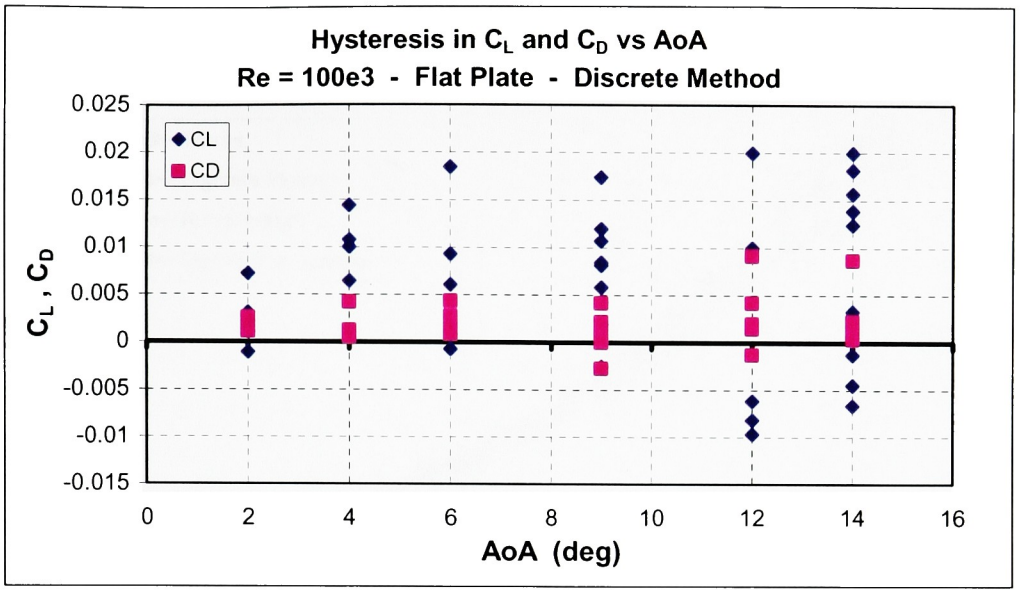

Figure 7-6 Hysteresis data used to estimate bias error

From these plots, the total uncertainty in the measurements can be estimated. A similar approach with the run method showed higher uncertainty. These uncertainties are shown in Table 7-1.

Estimated Experimental Uncertainty			
	Discrete	Run	Mechanical
C_L =	+/- 0.03	+/- 0.05	+/- 0.01
C_D =	+/- 0.007	+/- 0.01	+/- 0.01

Table 7-1 Experimental uncertainty

Figure 7-7 shows uncertainty bars on a plot of C_D of the flat plate. Larger plots of C_D and C_L uncertainty are available in Appendix B for greater clarity.

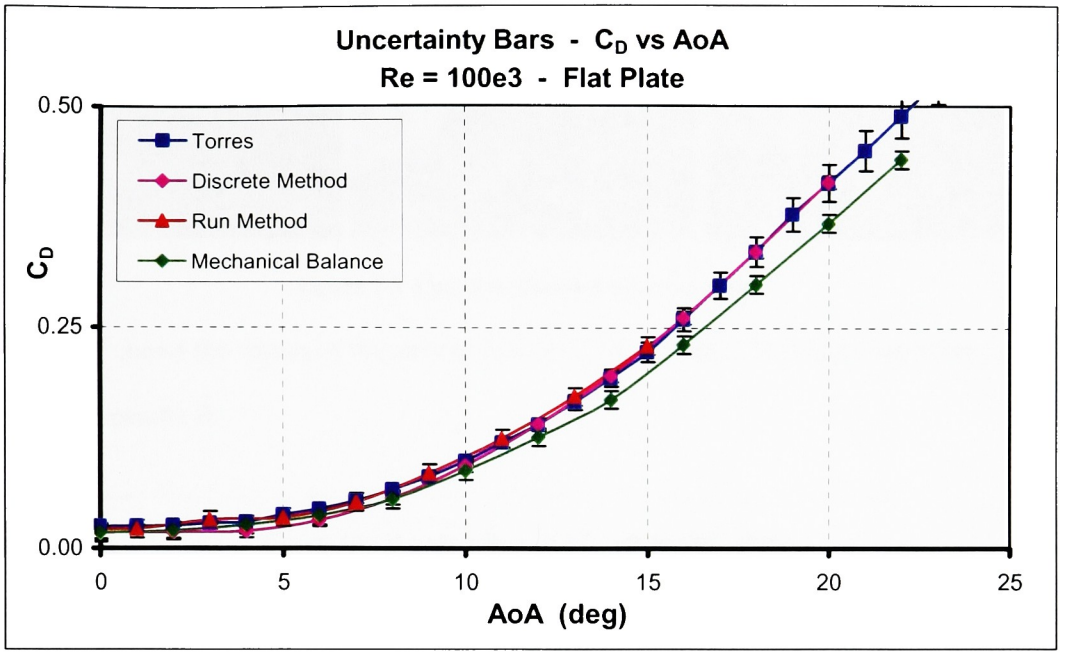

Figure 7-7 Uncertainty bars for C_D vs AoA of flat plate

7.2 Drag Validation

The idea of the drag tripod is by far the most unique aspect of the load cell balance design, and was therefore subjected to further testing and verification. Well established, widely accepted results for the drag testing of several simple shapes exist in available literature. The balance was tested using three simple shapes and compared to results published by Hoerner [16].These models were a 13 x 1 inch diameter cylinder, a 3 inch diameter disc and a 3.75 inch diameter sphere. Figure 7-8 shows the models as tested. Each was tested over a range of velocities expected in MAV testing. These velocities also corresponded to the Reynolds number regions that the comparative published data presents.

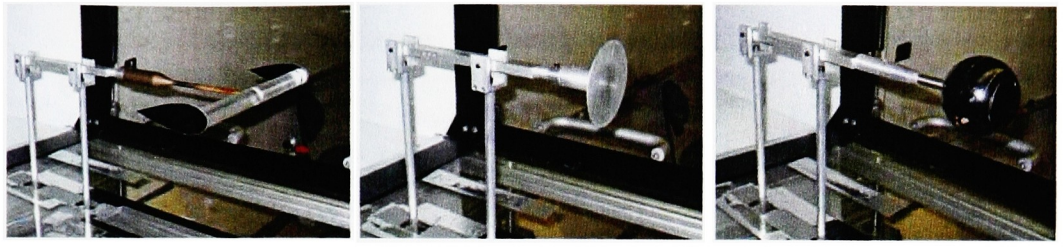

Figure 7-8 Cylinder, disc and sphere models

Figure 7-9 shows the results of the testing with the 3.75 inch disc. This and other plots can be seen in Appendix B.

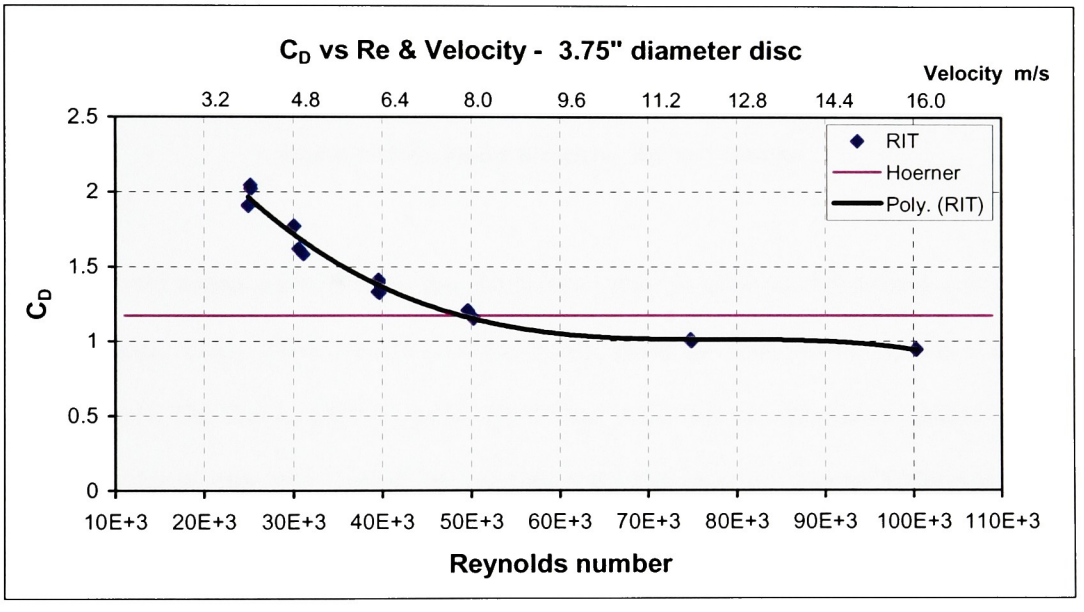

Figure 7-9 Drag results from disc testing

This plot shows an interesting result. At lower Reynolds numbers (speeds < 7 m/s) the balance over-predicts drag by a significant margin. At higher Reynolds numbers the balance slightly under-predicts drag. Looking at the results from all three models in Figure 7-10, this trend is confirmed.

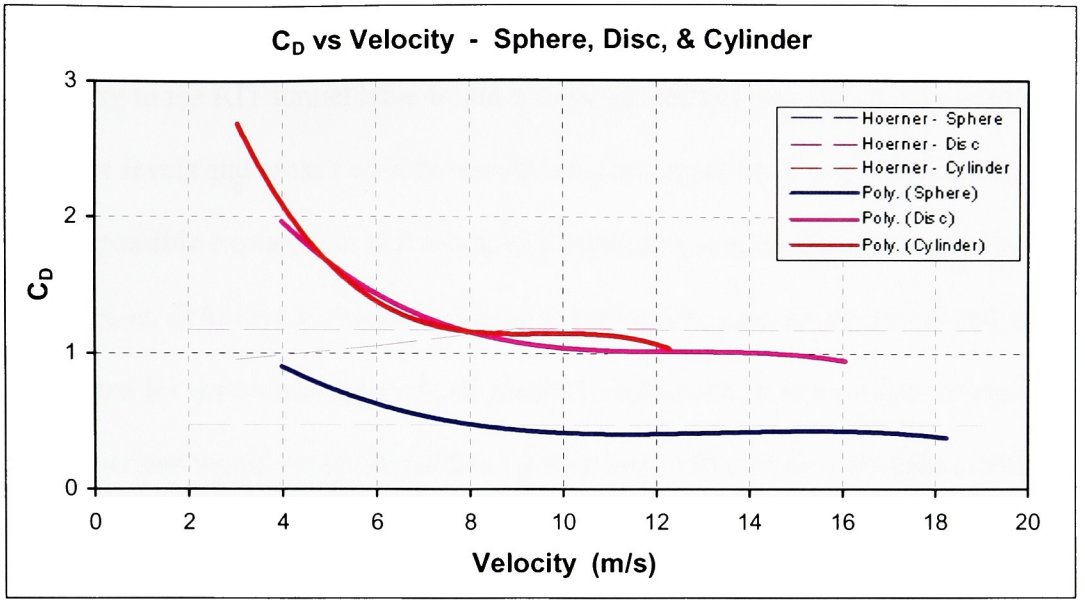

Figure 7-10 C_D results for sphere, disc and cylinder

It would appear from this plot that the balance should not be used at speeds lower than approximately 7 m/s. There are two probable explanations for the erroneous results at the lower speeds. The first is that the quality of the flow in the test section at slow speeds is poor. It is likely that at very slow speeds there are large separations of the flow as it enters the test section. If the model, or the dynamic pressure measuring pitot-tube, is affected by these large errors would result. The second explanation is the inability of the instrumentation to accurately measure the small quantities of force and pressure at the slow speeds. Specifically, the pressure transducer measuring dynamic pressure may be inaccurate at the very small pressure differences due to only a few m/s of velocity. Regardless, it is obvious the wind tunnel/balance system as designed cannot be used for testing below 7 m/s. This should not impact the majority of MAV testing however because most involve speeds higher than this.

The slight discrepancy at higher Reynolds numbers / velocities also has two likely explanations. The most likely cause is once again the quality of the flow. Past studies of the flow quality in the RIT tunnel have found it to be acceptable, but less than desirable. Turbulence levels and cross / up-flow would have an impact on any data collected.
A second possible explanation is the lack of a correction scheme for the wind tunnel. Despite past efforts, no definitive correction scheme has ever been completely developed and implemented for the tunnel. As such, all results in this research remain uncorrected. While these corrections would probably not have a very large effect, they may help explain the discrepancy between collected and published data.

7.3 Momentum Drag Experiment

As stated, one of the goals of this project was to construct a balance for use not only by graduate students, but for undergraduate studies as well. To this end, an undergraduate Fluids class [4] has already made use of the load cell balance. The lab experiment consisted of using the balance and the cylinder model discussed earlier to measure drag in two different ways. The students measured drag via the balance output reading; and compared this to a momentum drag calculation determined by analyzing the velocity profile behind the model. One lab section's results appear in Table 7-2.

	Measured by balance	Calculated by momentum	% Diff
F_D =	50.9 g	52.5 g	3.07%
C_D =	1.21	1.25	2.75%

Table 7-2 Momentum drag experiment 30ft/s

In the past, this lab has utilized the NK Mini-6 Sensor described in Section 1.1.1. With this system, a percentage difference of over twenty was common. With the new load cell balance the students are capable of achieving less than 5% difference between their calculations and the "actual" drag read by the balance system. This constitutes a drastic improvement in the capabilities of the Wind Tunnel Lab with respect to undergraduate research and education.

7.4 RIT Thnikkaman MAV Testing

With lift and drag verified as working properly by prior testing, the final testing performed with the load cell balance was of the RIT *Thnikkaman* Micro Air Vehicle (Figure 7-11). This platform was developed and flown over the course of the 2003-2004 academic year.

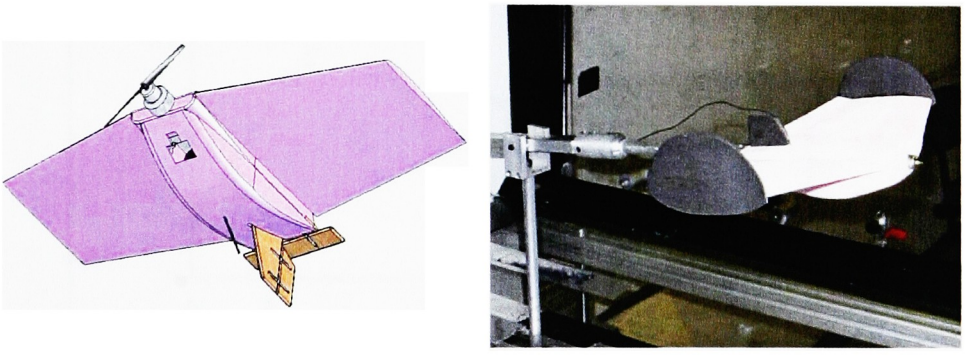

Figure 7-11 RIT Thnikkaman MAV computer model and in testing

The MAV was developed with little experimental data because the load cell balance was not functional until the end of the academic year. The MAV was tested several months later to

verify the project team's assumptions and flight performance predictions. Also, the testing will show the applicability of the balance to testing full-size MAVs.

Testing was performed at Reynolds numbers of 70,000 and 100,000. These correspond (assuming standard conditions) to the predicted velocity envelope of the vehicle of between 7.5 to 11 m/s. The MAV was tested using the run method, the experimental setup and the data analysis techniques described in previous sections. Figure 7-12 and Figure 7-13 show some of the results from this testing.

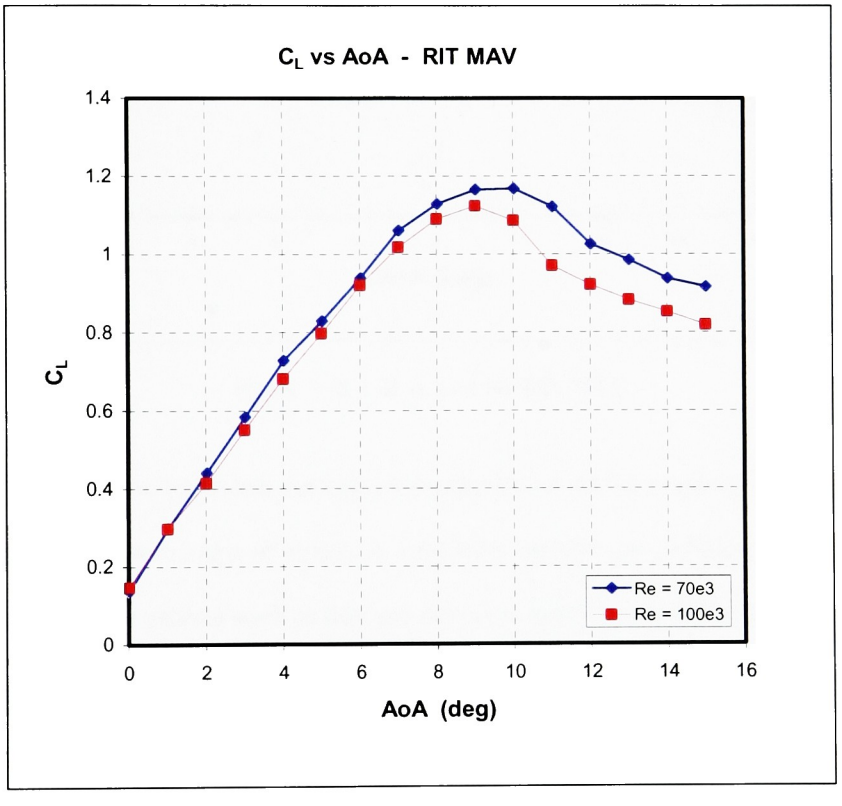

Figure 7-12 C_L vs AoA for Thnikkaman MAV

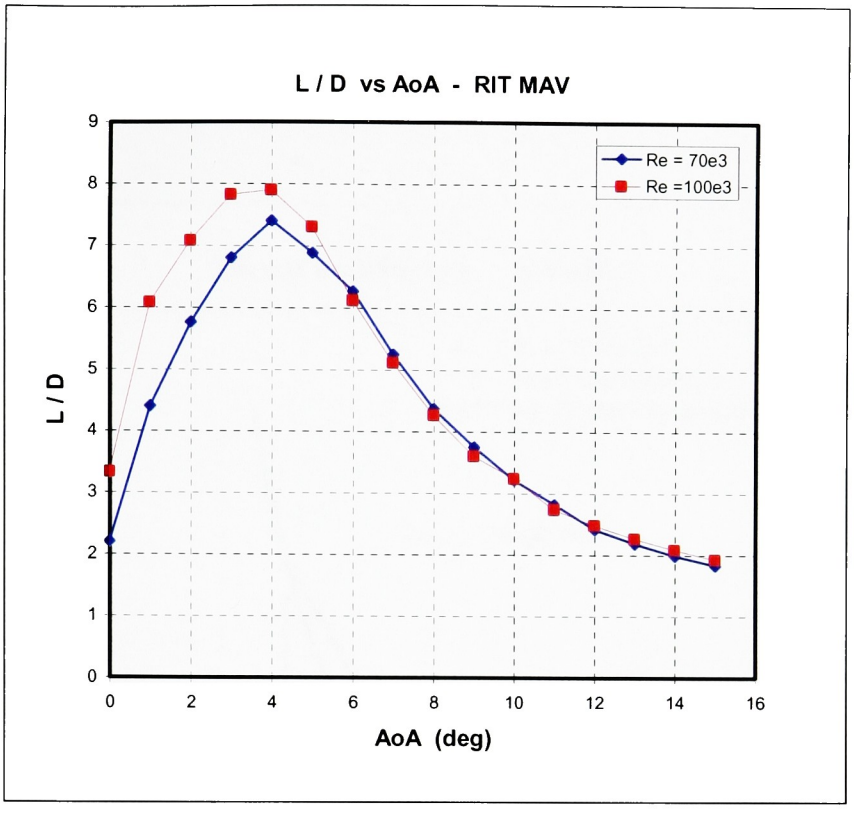

Figure 7-13 L/D vs AoA for RIT MAV

The results are as expected. An approximately linear lift curve gives way to stall at approximately 9 degrees angle of attack. A maximum aerodynamic efficiency (L/D) of 8 is very reasonable for a vehicle such as this and occurs at approximately the same angle for both Reynolds numbers. Using these results, a performance analysis was conducted on the MAV design to see how well the experimental results match with the actual flight testing experience. During flight testing, of which the author took part, the RIT MAV flew rather slowly, with a very obvious high AoA. While never fully quantified, it was agreed (through direct experience and video taped timing) the vehicle flew at approximately 20 miles per hour. Static thrust testing showed the maximum thrust available from the powerplant to be 26

grams. Using this information, and the fact that propeller efficiency drops rapidly as speed increases for these small aircraft, the plot in Figure 7-14 was developed.

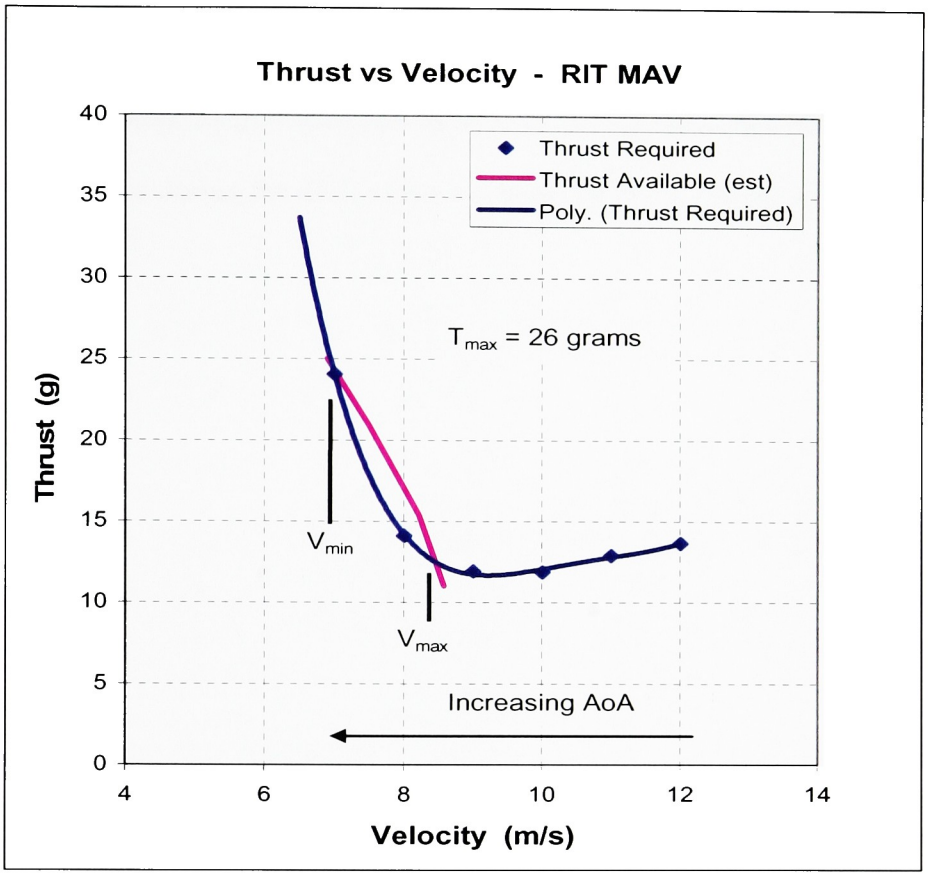

Figure 7-14 RIT MAV performance plot

The thrust required curve was developed from standard equations [17], and the thrust available curve developed from the experimental thrust tests and flight experience. The plot shows that the MAV operated on the low end of the thrust curve, meaning it flew very slowly (close to stall), and at a high angle of attack. In full video-reconnaissance configuration, the vehicle weighed 95 grams. It was due to the extra weight from this equipment that MAV

operated so close to the edge. With weight taken off, the thrust required curve shifts down, and the vehicle flew faster, at a lower AoA and with greater efficiency.

It was found that the project team that constructed the MAV slightly overestimated lift and underestimated drag from their purely analytical approach. This is what caused marginal MAV performance and the vehicle's tendency to stall unexpectedly. Future teams will benefit from the use of the new load cell balance by having hard experimental data for vehicle performance during the design phase, instead of relying solely on analytical estimates.

8 Conclusions & Recommendations

Through the methods and research detailed, two balances have been designed and fabricated for the specific purpose of testing Micro Air Vehicles. The first balance consists of a modified version of previous work at RIT and relies solely on mechanical means to independently determine lift and drag. A second balance employs a unique external balance design and the incorporation of four load cells to capture lift and drag simultaneously. Theoretically able to also determine pitching moment, at this time the uncertainty in pitching moment results is too great to determine useful results. Some of the benefits and drawbacks to each balance are detailed below.

- Mechanical Balance
  - Benefits
    - Excellent repeatability and resolution
    - Very simple design
    - Inexpensive, easily repaired
  - Drawbacks
    - Must measure lift and drag in separate runs
    - Cannot capture pitching moment
    - Can be tiresome to use
    - Cannot be used near stall angle or dynamic effects

It was found that the modifications to the mechanical balance allowed data from MAV scale models to be captured with excellent repeatability and resolution. Comparing to published data, the balance reported values generally within 10%. At lower angles of attack the balance proved more accurate.

At higher angles, particularly near stall, the balance had a tendency to oscillate wildly and not return to the equilibrium position necessary to take a measurement. Dynamic effects at these higher angles most likely change the force on the model too rapidly for equilibrium to be reached. This drawback most of all limits the use of the balance in certain experiments.

Another serious drawback to use of the mechanical balance is operator fatigue. Because the balance is mounted to the top of the wind tunnel and uses very small weights and distances to determine measurements it can be very tiresome for an experimenter to use for extend periods of time. Future use of the mechanical balance will most likely be confined to certain unique small-scale experiments that desire very small uncertainties but are unaffected by the drawbacks of its use.

- Load Cell Balance
  - Benefits
    - Computer integration and control, future full-automation capability
    - Measures all longitudinal data simultaneously
    - With additional work, is capable of measuring pitching moment
    - Decent resolution and repeatability
    - Can be outfitted to measure different ranges by changing load cells
  - Drawbacks
    - Resolution suffers compared to mechanical balance
    - System can be fragile, particularly load cells
    - More costly to repair, but at ≈ $2,600 still far less expensive than commercial alternatives

Except for the current inability to accurately determine pitching moment, the load cell balance has met all the goals it was designed to meet. Its computer integration and control make it user-friendly and fit into the overall plan of automating data collection and experiments in the Wind Tunnel Lab. Furthermore, it can be modified to measure different ranges of forces by simply changing the load cells used. The current load cells and setup have been shown to have the degree of resolution and repeatability to accurately measure forces on MAVs.

The implementation of these balances is the first step on a long path of improvement and development of the RIT Subsonic Wind Tunnel. If it is to succeed, the emerging RIT

Micro Air Vehicle Program demands a facility capable of supporting its needs for accurate experimental data. Future work on both the balances and the tunnel facility itself is needed.

It is recommended that the mechanical balance be left in its current form and be used in the unique situations it is best suited for or as experimental programs deem it necessary. It is undoubtedly an excellent tool for determining very small lift and drag forces and will certainly see some use in the future. The potential associated with the load cell balance, however, is much greater.

The first step in any future work with this balance should be a troubleshooting program to determine the cause of the errors in capturing pitching moment and correct them. This will not be an insignificant task because of the considerable amount of time already invested in it. One suggested design change is shown in Figure 8-1.

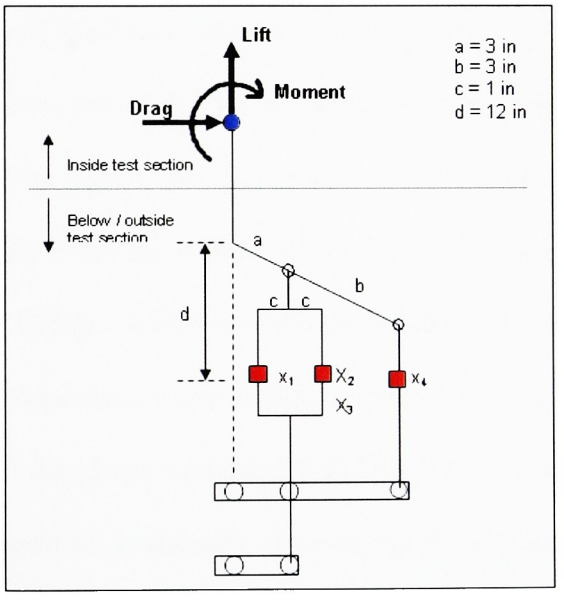

Figure 8-1 Suggested design change for load cell balance

With this design, dimensions "a" and "b" are shortened and the model alone is within the test section. This would serve to reduce interference errors and tare errors. With these

modifications and perhaps some unforeseen design/analysis changes, pitching moment can be fixed.

Another focus of future work could be on refining the LabVIEW setup. Incorporation of other instrumentation, such as the AoA sensor, the motorized model positioning system, and tunnel speed controller would be of great benefit to all users of the system. Also, a more thorough analysis of the digital filtering may determine modifications that yield better accuracy and uncertainty. Finally, it is recommended that all future work pay close attention to the calibration of the system as a whole. Careful calibration of the system, and the load cell tripod in particular, is necessary to reduce the effects of asymmetric loading and assembly.

With all of these modifications to the balance, it is also important to make certain improvements to the tunnel itself to ensure the highest confidence in the experimental data. A final determination of flow quality must be undertaken and the required adjustments made to bring test section flow to its highest possible quality. Also, a final system of determining wind tunnel corrections for blockage effects, wall effects, etc, must be formulated and made available to tunnel users. While internal use of experimental data without these advances is certainly acceptable and necessary, without these improvements to the facility it is difficult to publish any experimental data from the tunnel with a high degree of confidence.

RIT is ideally positioned to contribute in a meaningful, even leading, manner to the growing Micro Air Vehicle community. The wind tunnel balances developed through this research give the students and faculty of RIT excellent tools for experimentally investigating the field of aerodynamics on an MAV scale. With further work on the balances and the facility the range of research opportunities will continue to grow.

Appendix A - LabVIEW Block Diagram

A highly detailed depiction and description of the block diagram would take dozens of pages and be unnecessary. On the pages of this appendix are sectioned pieces of the block diagram and notes to give the reader a general idea of what the diagram consists of and how the VI functions.

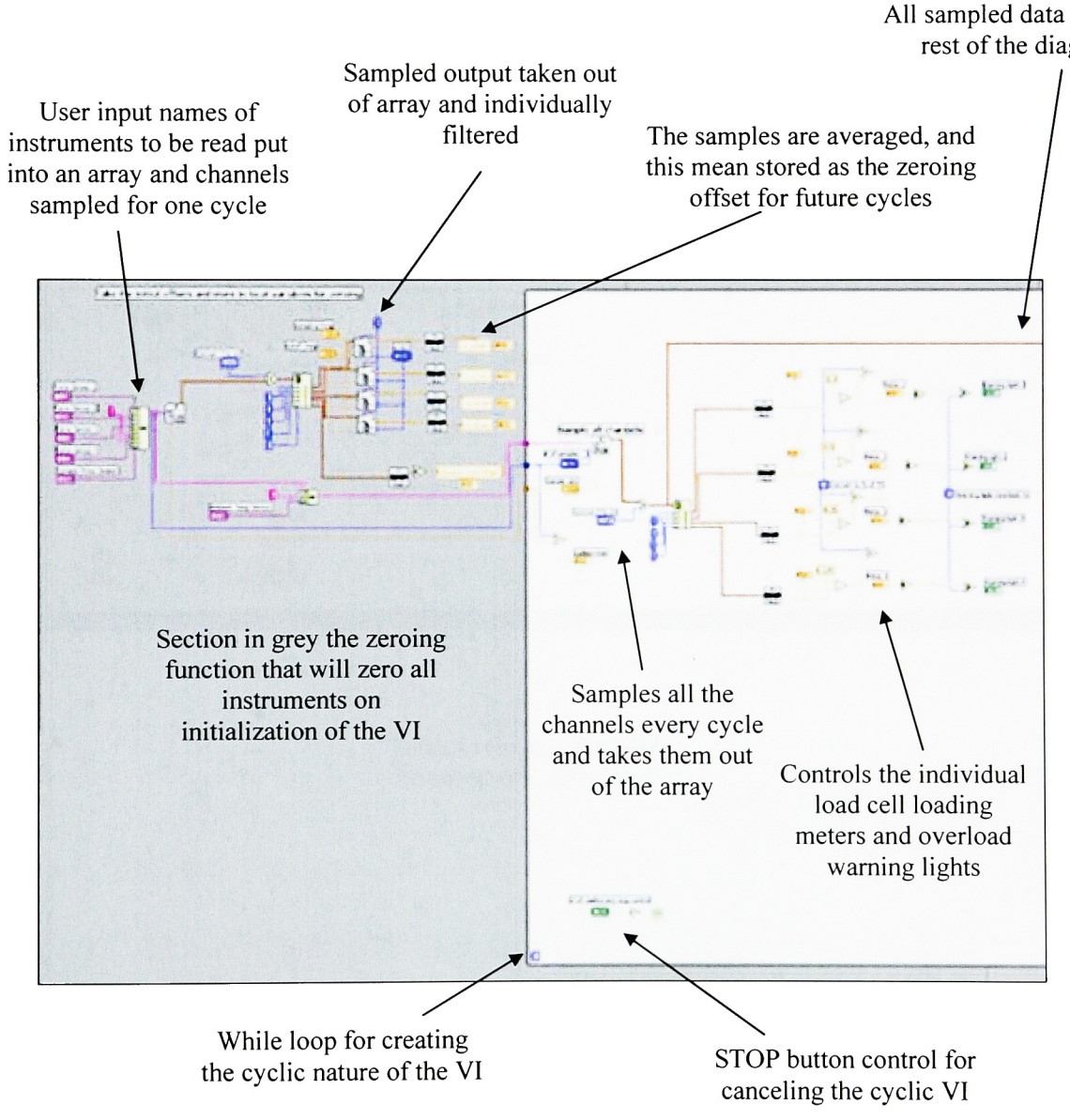

Block Diagram 1 of 4

Load cell data put through low-pass filters and the zero-offset subtracted off

Lift, drag and pitching moment calculated using equations from Section 5

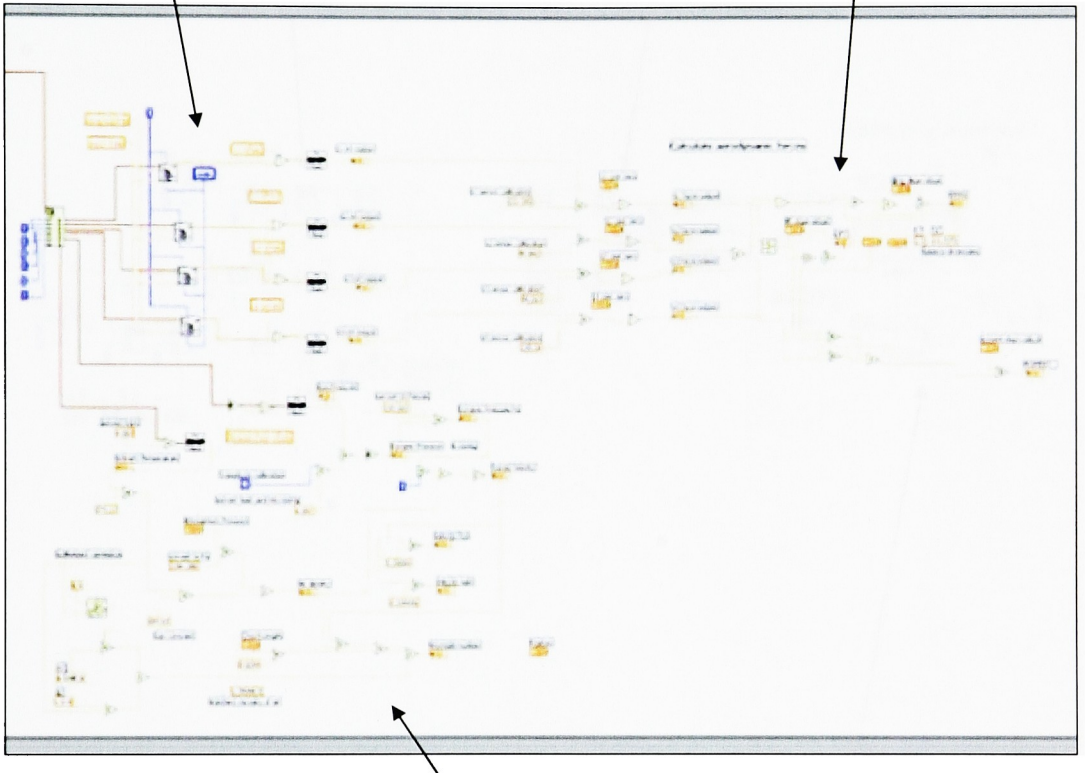

Tunnel velocity, Reynolds number, etc, calculated

Block Diagram 2 of 4

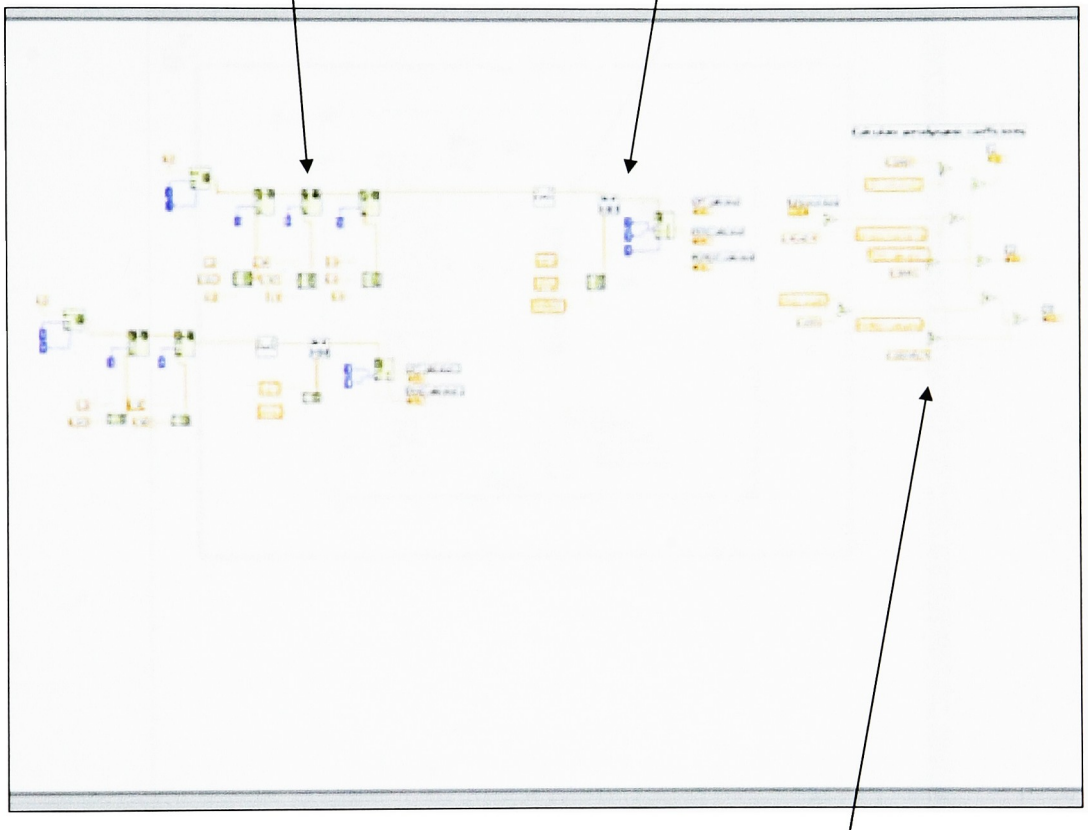

Block Diagram 3 of 4

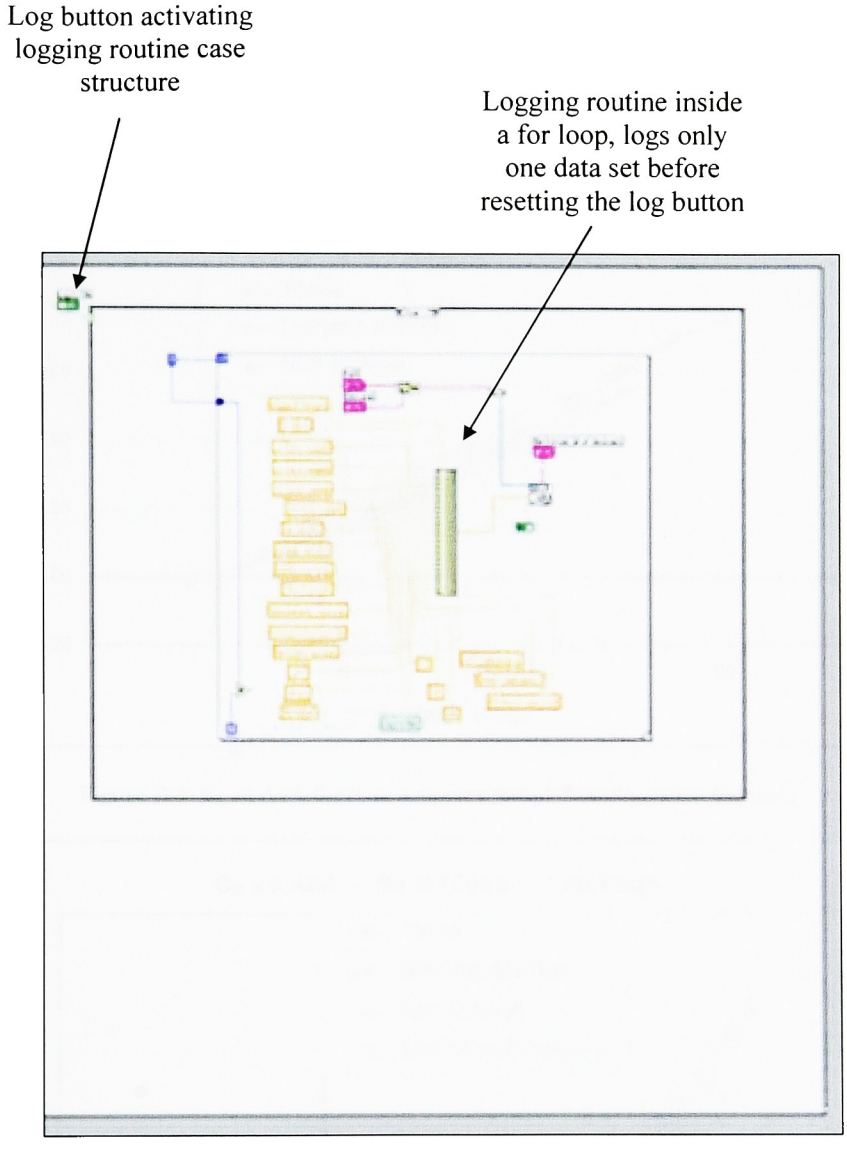

Block Diagram 4 of 4

Appendix B - Experimental Results

All plots and pertinent experimental results are republished in this appendix in larger format for easier readability.

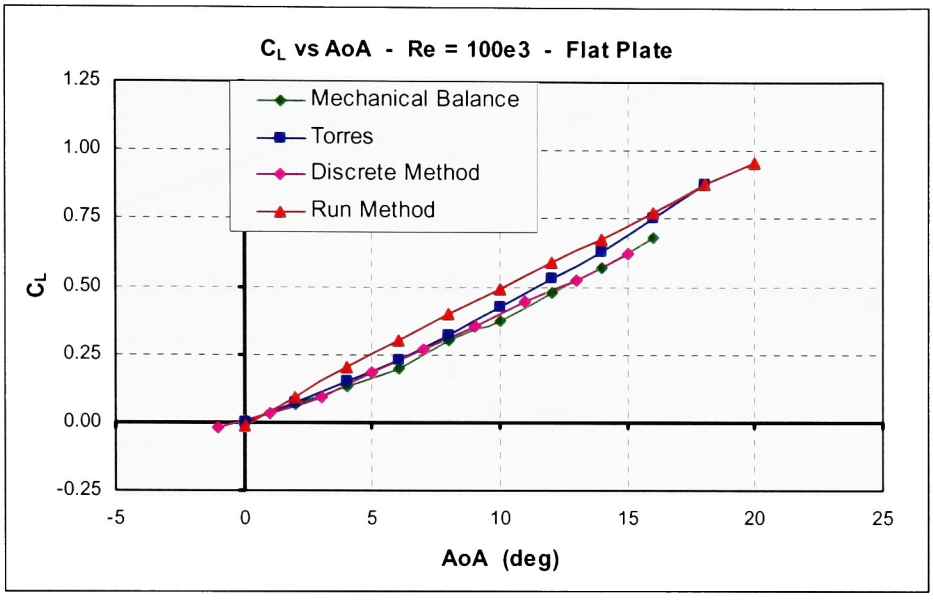

Figure B-1 C_L vs AoA for 8 inch square flat plate testing with balances

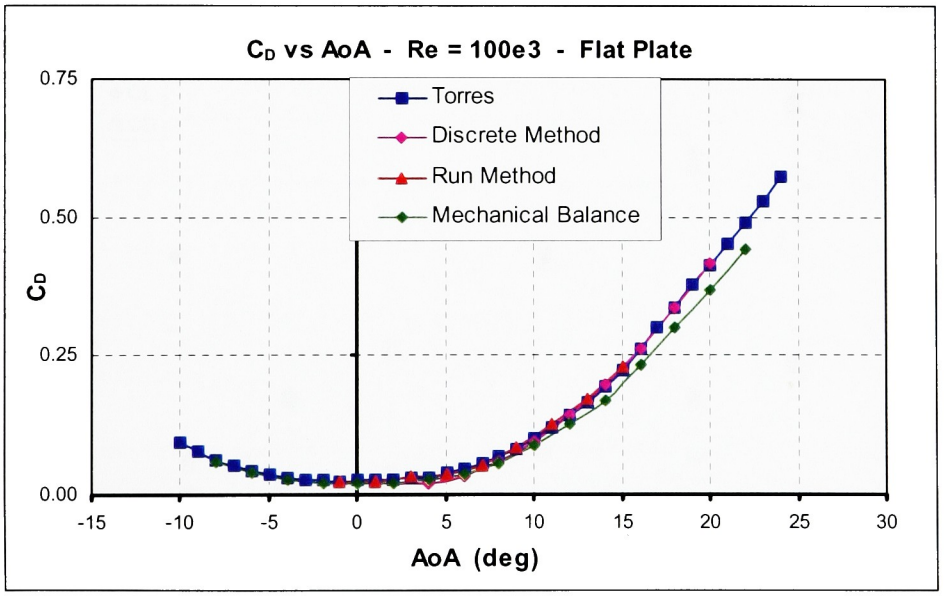

Figure B-2 C_D vs AoA for 8 inch square flat plate testing with balances

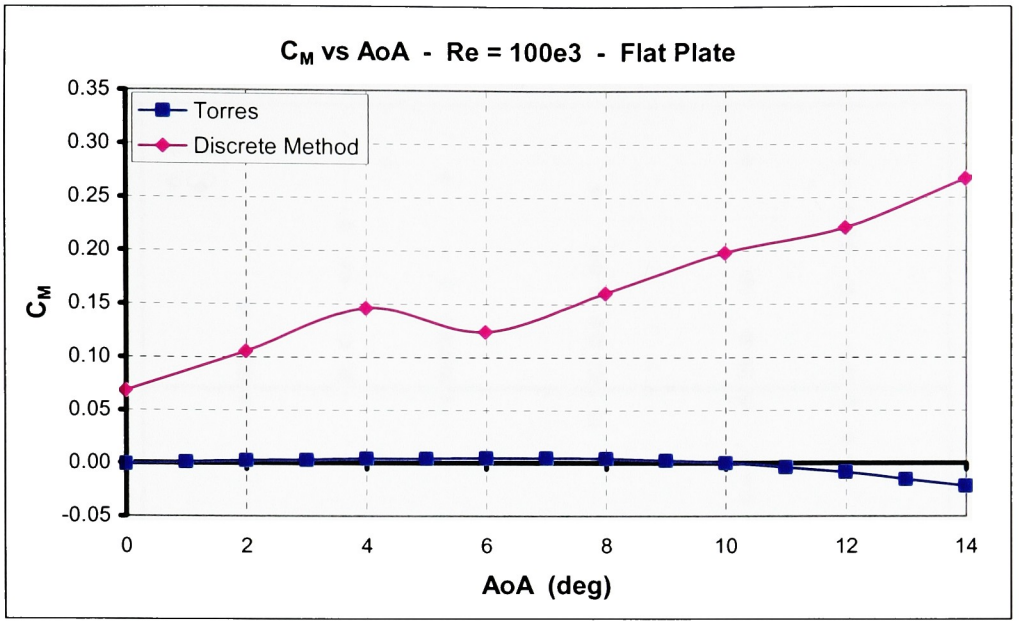

Figure B-3 C_M vs AoA for 8 inch square flat plate testing with load cell balance

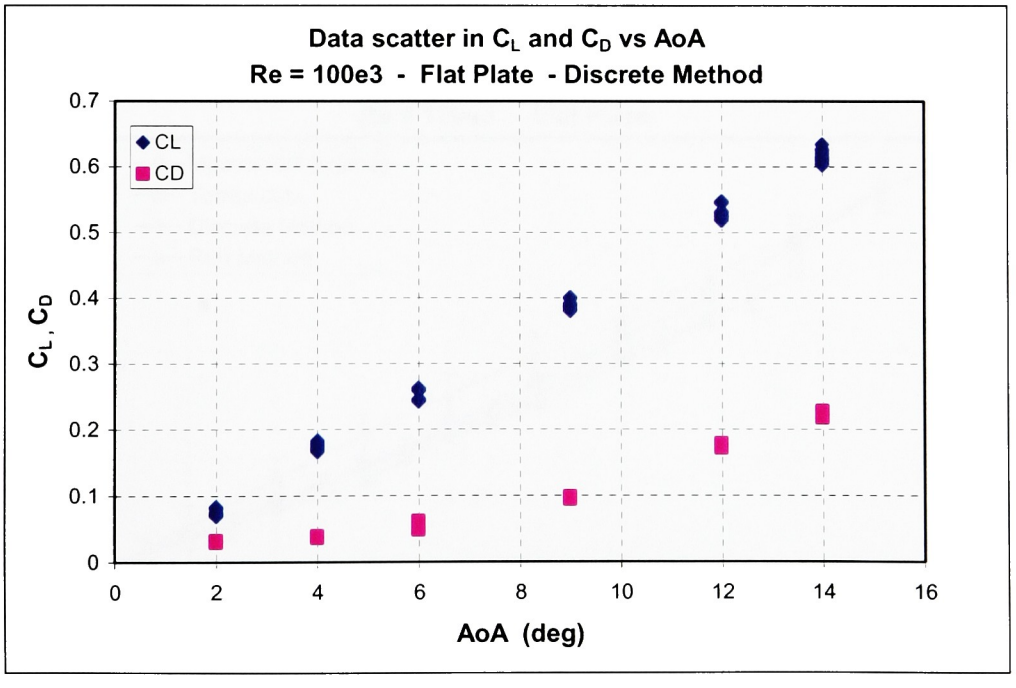

Figure B-4 Data scatter from several runs of flat plate with discrete method showing precision of data

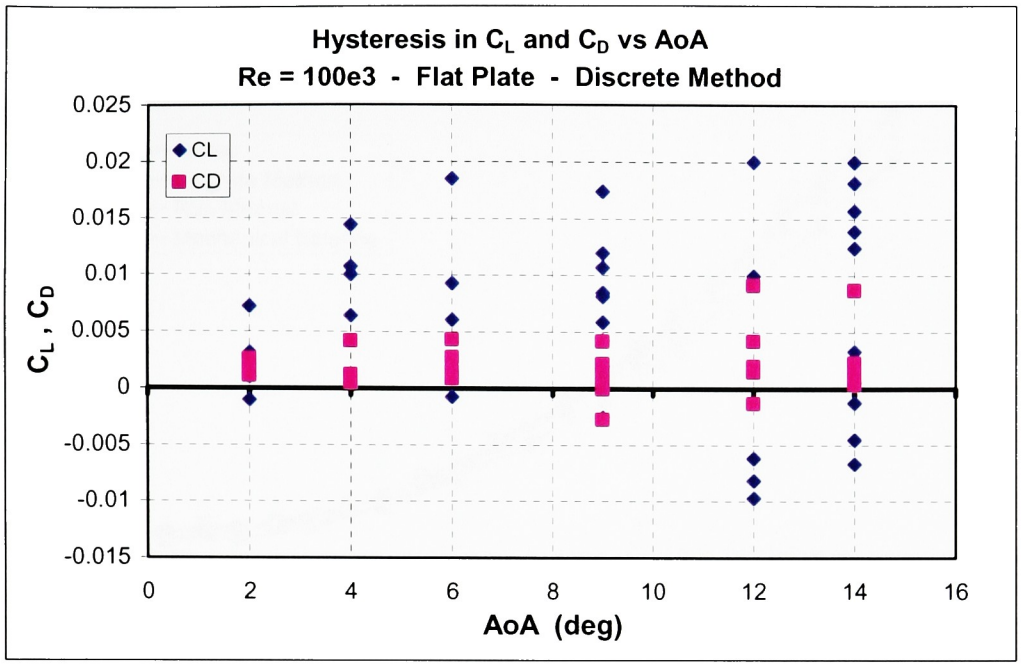

Figure B-5 Hysteresis from flat plate testing with load cell balance, used to evaluate bias error

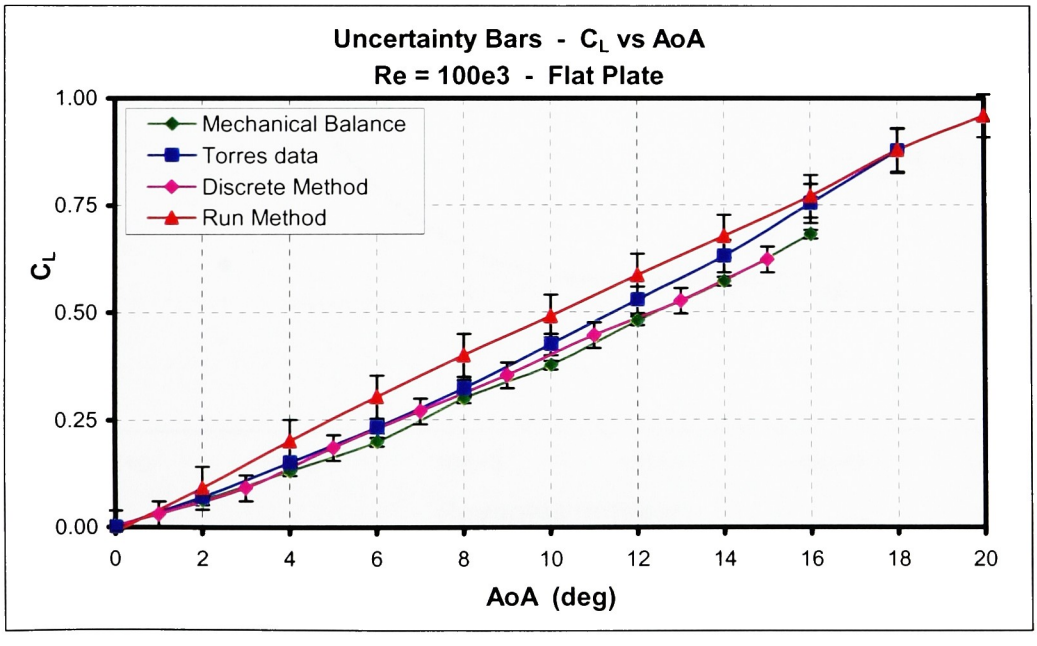

Figure B-6 Error bars for C_L vs AoA of flat plate testing

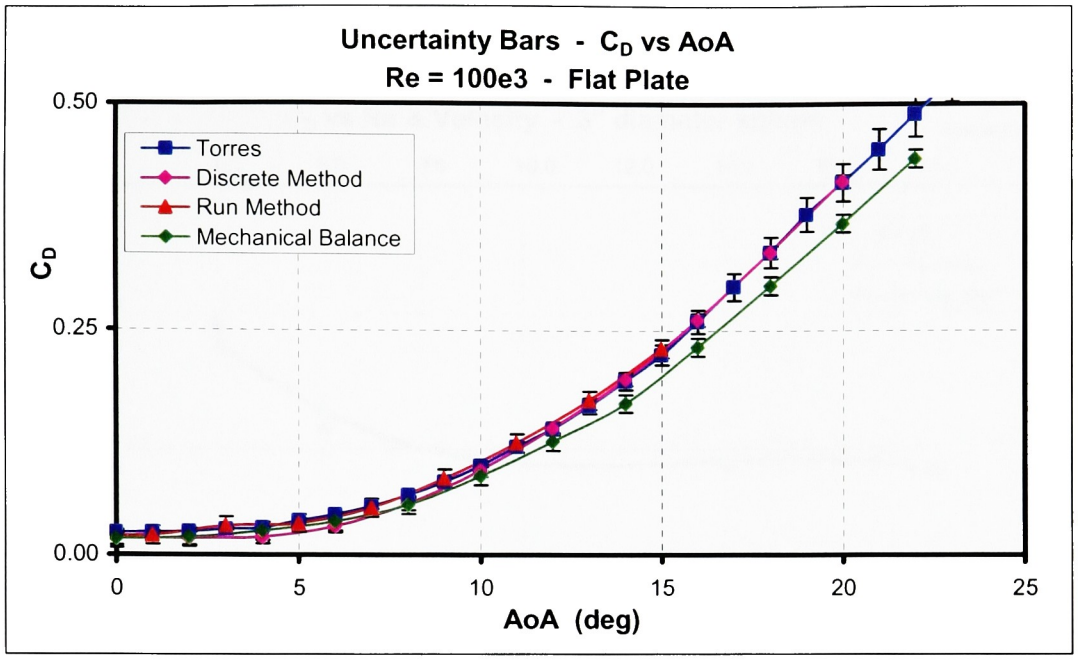

Figure B-7 Error bars for C_D vs AoA of flat plate testing

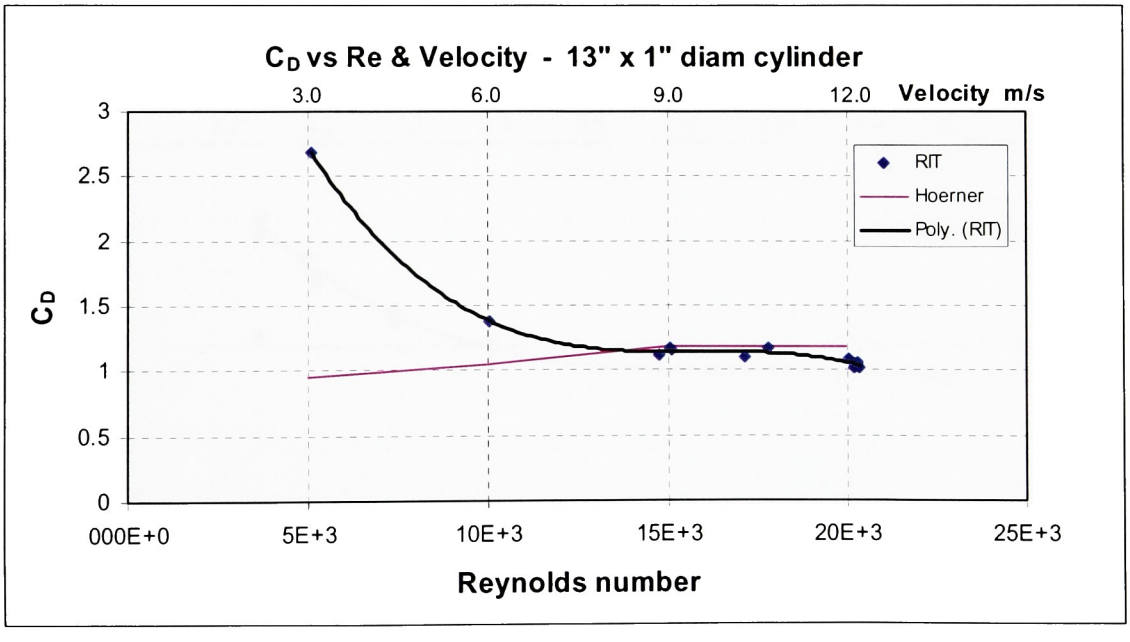

Figure B-8 Drag of cylinder vs Reynolds number and velocity of tunnel

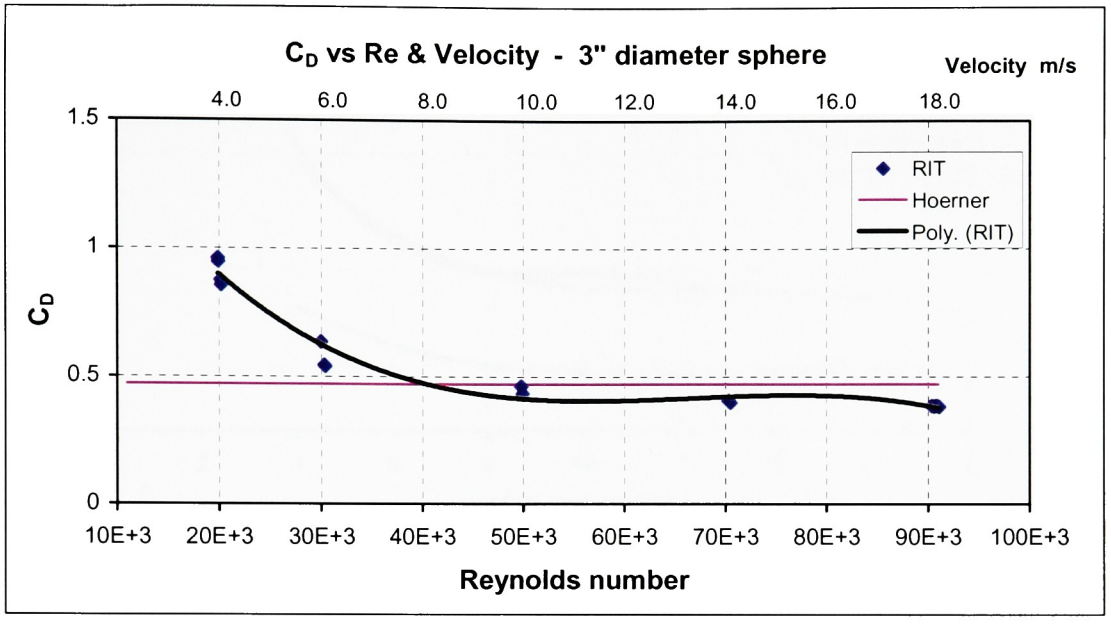

Figure B-9 Drag of sphere vs Reynolds number and velocity of tunnel

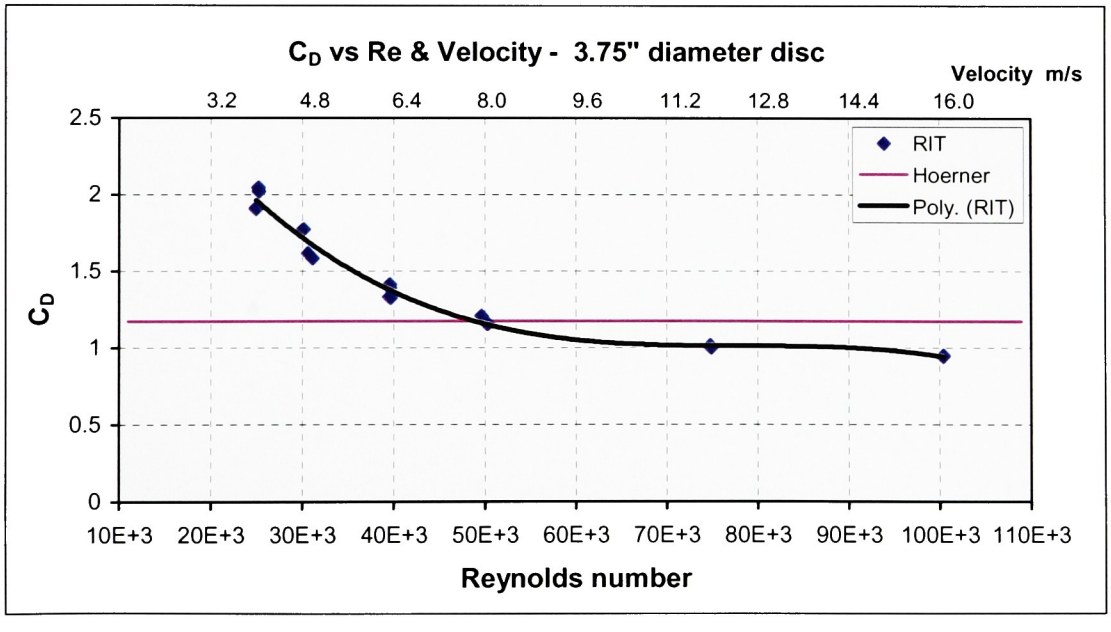

Figure B-10 Drag of disc vs Reynolds number and velocity of tunnel

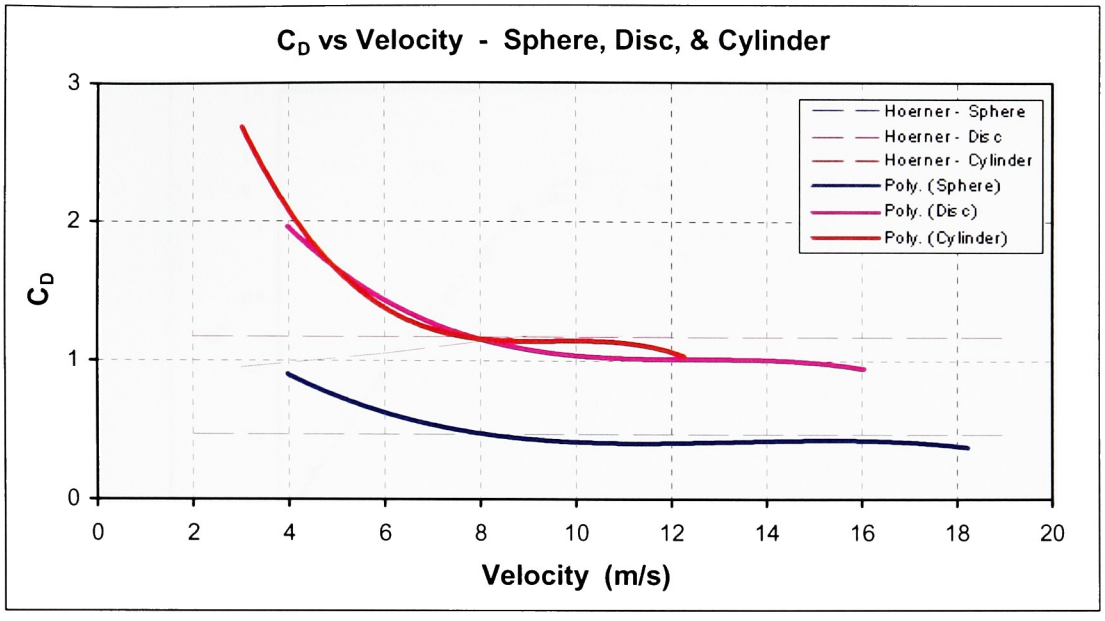

Figure B-11 Drag results with load cell balance compared to drag results from Hoerner

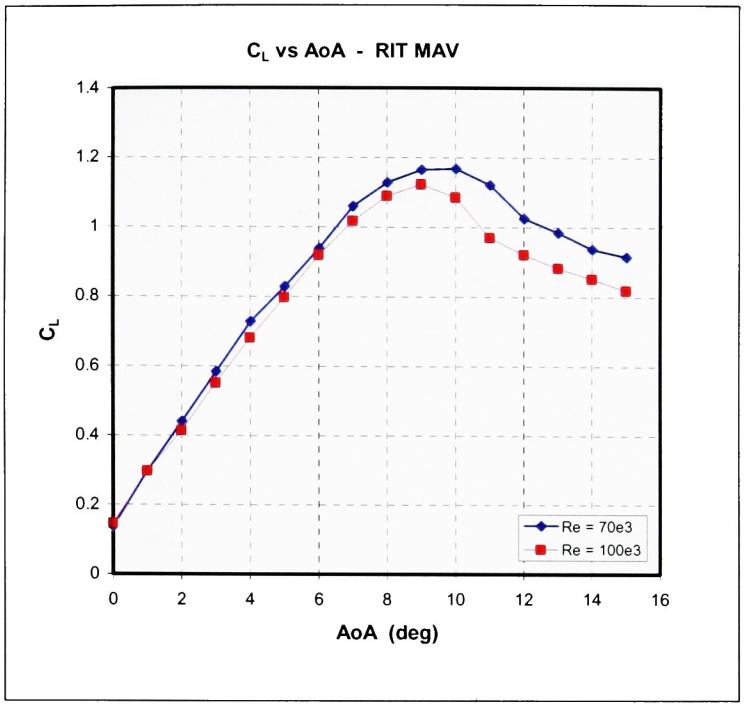

Figure B-12 C_L vs AoA for RIT MAV using load cell balance

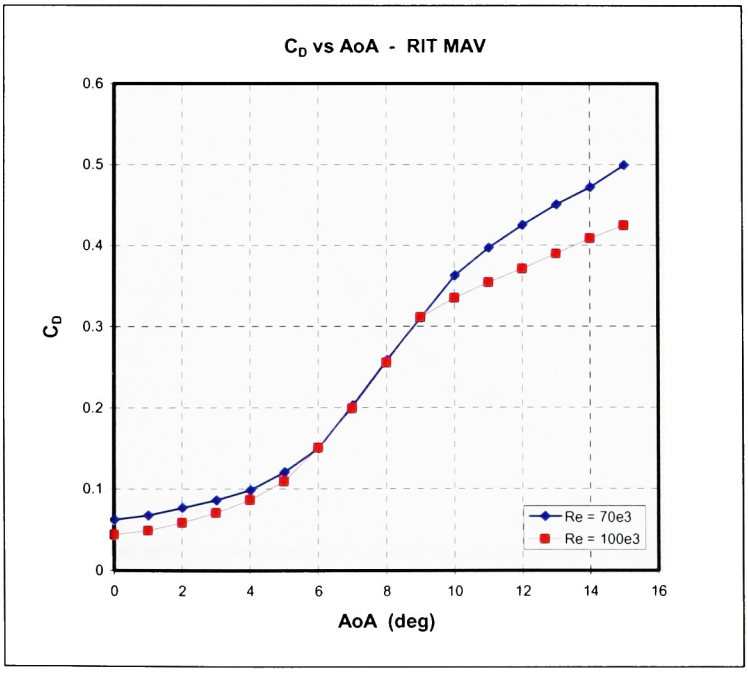

Figure B-13 C_D vs AoA for RIT MAV using load cell balance

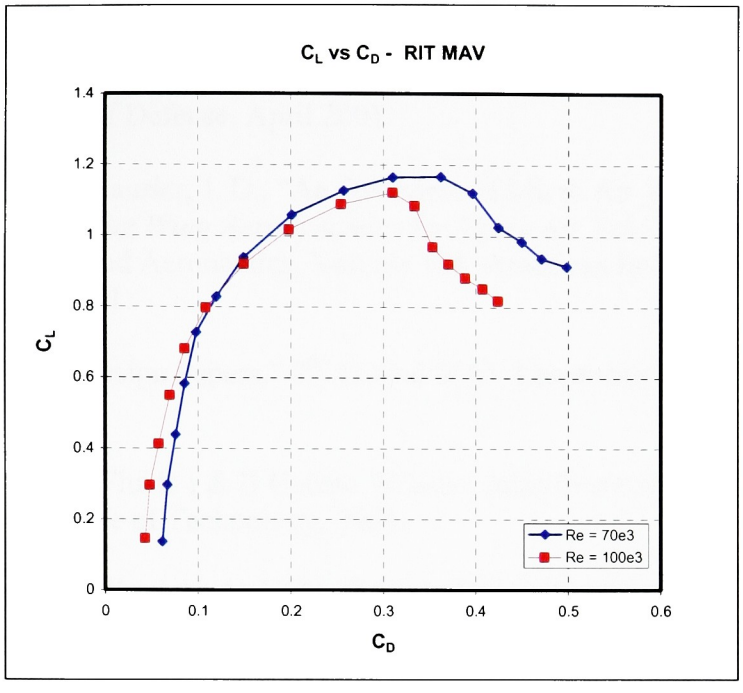

Figure B-14 C_L vs C_D for RIT MAV using load cell balance

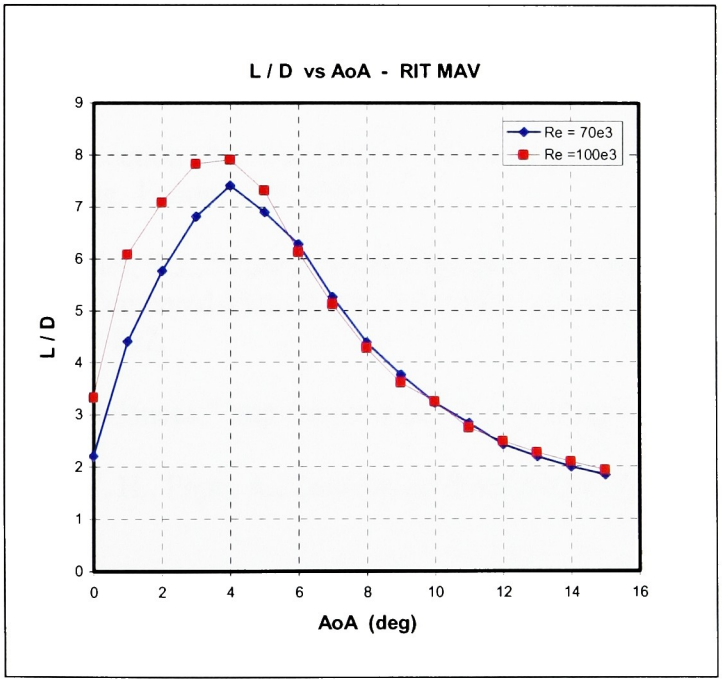

Figure B-15 L/D vs AoA for RIT MAV using load cell balance

References

1. "Unmanned Aerial Vehicles Roadmap: 2000-2025," Office of the Secretary of Defense, US Department of Defense, April 2001.

2. Mueller, T. J. and DeLaurier, J. D., "An Overview of Micro Air Vehicle Aerodynamics," *Fixed and Flapping Wing Aerodynamics for Micro Air Vehicle Applications*, Progress in Astronautics and Aeronautics, Volume 195, American Institute of Aeronautics and Astronautics, 2001.

3. "Micro Air Vehicle Design Papers," 8th Annual MAV Competition, University of Arizona, 2004.

4. Steinke, M., Thermal Fluids I & II Course Website, http://www.rit.edu/~meseme/, Rochester Institute of Technology, 2004.

5. Boughton, S., et al, "Micro Air Vehicle Airframe Design", *Proceedings of the 2002-2003 RIT Multi-Disciplinary Senior Design Conference*, Rochester, NY, 2003.

6. Abe, C., "Aerodynamic Force and Moment Balance Design, Fabrication and Testing for use in Low Reynolds Flow Applications," Thesis: Rochester Institute of Technology, 2003.

7. Laitone, E. V., "Wind Tunnel Tests of Wings and Rings at Low Reynolds Numbers," University of California, Berkeley, Califorina, 2001.

8. Sunada et al, "Airfoil Section Characteristics at a Low Reynolds Number," *Journal of Fluids Engineering, Volume 119*, 1997.

9. Pelletier, A., and Mueller, T.J., "Low Reynolds Number Aerodynamics of Low-Aspect-Ratio, Thin/Flat/Cambered-Plate Wings," *Journal of Aircraft*, Vol. 37, No. 5., Sept-Oct 2000, pp. 825-832.

10. "AeroLab Inc Sting Balances," http://www.aerolab.com/sting.htm, 2004.

11. Barlow, J. B., Rae, W. H., Pope, A., *Low-Speed Wind Tunnel Testing*, Wiley, New York, 1999.

12. Selig, M. et al, "Summary of Low Speed Airfoil Data, Volume 3," University of Illinois at Urbana-Champaign, Soartech Publications, March 1998.

13. Popeil, R., *Showcase Rotisserie Oven*, http://www.ronco.com, Ronco, 2004.

14. "Assessment of Experimental Uncertainty with Application to Wind Tunnel Testing," American Institute of Astronautics and Aeronautics, Standard S-071A-1999, 1999.

15. Torres, G. E., and Mueller, T. J., "Aerodynamic Characteristics of Low Aspect Ratio Wings at Low Reynolds Numbers," *Fixed and Flapping Wing Aerodynamics for Micro Air Vehicle Applications*, Progress in Astronautics and Aeronautics, Volume 195, American Institute of Aeronautics and Astronautics, 2001.

16. Hoerner, S. F., *Fluid-Dynamic Drag*, Hoerner Fluid Dynamics, Brick Town, NJ, 1975, pp. 3-8 – 3-16.

17. Anderson, J. D., *Introduction to Flight*, Fourth Edition, McGraw-Hill, New York, 2000.